

Enormous Cloud Cover on Venus observed by Akatsuki's IR2 data recovered by Restoration-by-Deconvolution (RD) method

Choon Wei Vun (✉ anthonyvun@hotmail.com)

〒〒〒〒〒〒/ The Graduate University for Advanced Studies, SOKENDAI
4449-0737

<https://orcid.org/0000-0003-4449-0737>

Takehiko Satoh

Institute of Space and Astronautical Science (ISAS/JAXA)

Takao M. Sato

Hokkaido Information University

Takeshi Horinouchi

Hokkaido University

Full paper

Keywords: Venus, Akatsuki, Atmosphere, Aerosols, Near-Infrared, Image Processing

Posted Date: May 11th, 2020

DOI: <https://doi.org/10.21203/rs.3.rs-26756/v1>

License:   This work is licensed under a Creative Commons Attribution 4.0 International License.

[Read Full License](#)

1 **Title: Enormous Cloud Cover on Venus observed by Akatsuki's**
2 **IR2 data recovered by Restoration-by-Deconvolution (RD) method**

3

4 Author 1: Choon Wei Vun, Department of Space and Astronautical Science, The Graduate
5 University for Advanced Studies, SOKENDAI, 3-1-1 Yoshinodai, Chuo-ku, Sagamihara,
6 Kanagawa 252-5210, Japan, anthonyvun@hotmail.com

7

8 Author 2: Takehiko Satoh, Institute of Space and Astronautical Science, Japan Aerospace
9 Exploration Agency, 3-1-1 Yoshinodai, Chuo-ku Sagamihara, Kanagawa 252-5210, Japan,
10 satoh@stp.isas.jaxa.jp

11

12 Author 3: Takao M. Sato, Space Information Center, Hokkaido Information University, 59-2,
13 Nishinopporo, Ebetsu, Hokkaido 069-8585, Japan, sato.takao@do-johodai.ac.jp

14

15 Author 4: Takeshi Horinouchi, Faculty of Environmental Earth Science, Hokkaido University,
16 Nishi 5 Kita, Kita 10, Kita-ku, Sapporo, Hokkaido 060-0810, Japan,
17 horinout@ees.hokudai.ac.jp

18

19 **Abstract**

20 We have developed a new method ‘Restoration by Deconvolution’ (RD) to restore nightside
21 photometry in the Akatsuki/IR2 images contaminated by spread light from intense dayside
22 crescent. With updated point spread function model for IR2 and incorporation of radiative
23 transfer computations, our RD-method is able to improve the photometric accuracy of nightside
24 emission data in both 2.26 μm and 1.735 μm filters. Exploiting the enhanced photometric
25 quality, the ‘Enormous Cloud Cover’ (ECC) features observed in both 2016-08-18 and 2016-
26 08-27 data have been investigated. Possible altitude variations in the ECC’s spatial variation
27 measurements from $z=52\text{km}$ up to $z=60\text{km}$ were found. The observations were interpreted that
28 ECC constituting of large sulfuric acid droplets (mean radius of 3.65 μm and the optical
29 thickness $\sim 7-9$) experience strong upwelling near the ECC front. This elevates the aerosols up
30 to $z=58-60\text{km}$, then subjected upon by strong downwelling forces the particles to sink by a
31 velocity $\sim -0.3\text{m/s}$. The analyses of physical properties and evolutionary behavior of the ECC
32 on both dates (08-18 and 08-27) suggest them to be recurring phenomena in the lower part of
33 Venus’ clouds.

34

35 **Keywords**

36 Venus, Akatsuki, Atmosphere, Aerosols, Near-Infrared, Image Processing

37

38 **1. Introduction**

39 Venus is shrouded by thick clouds of which structures have been explored by various
40 measurements: multiwavelength observations (imaging and spectroscopy), in-situ probe and
41 landers, and radio occultation. The clouds have significant influence in the energy budget,
42 meteorology, microphysical and chemical processes in the atmosphere. Past explorations by

43 Pioneer Venus (PV), Venera and Vega entry probes (Esposito et al, 1983) have discovered the
44 cloud's main deck situating in between ~47 to 70 km altitudes is vertically stratified into three
45 distinctive layers (upper, middle, and lower clouds) accompanied by tenuous hazes above and
46 below the cloud deck. The upper clouds observed by reflected sunlight are opaque and
47 featureless and exhibiting contrasts when observed in the ultraviolet regime (Pollack et al.,
48 1979). On the other hand, the middle and lower clouds (47.5-56.5km altitudes) can be probed
49 by infrared remote sensing to observe both dayside (Belton et al., 1991; Peralta et al., 2018)
50 and nightside (Allen & Crawford, 1984). The lower clouds are constantly being heated from
51 below by thermal radiation originating from the hot lower atmosphere and the ground. This
52 drives convection in the lower cloud layer (Imamura et al.2014, Baker et al., 1998) that
53 activates the microphysical processes of the cloud particles to go through condensation,
54 coagulation, and evaporation in this dynamical range (McGouldrick., 2017). Hence, the lower
55 clouds play the key role in contributing to the Venusian greenhouse effect, local radiative
56 energy balance, and cloud dynamics (Titov et al., 2018; McGouldrick et al., 2012).

57

58 Based on PV's Cloud Particle Size Spectrometer (LCPS) studies, measuring particle sizes upon
59 descent have evidenced the multimodal particle size distribution in the vertically stratified main
60 cloud layers (Knollenberg and Hunten, 1980). Particle distribution mode 3 ($\bar{r} = 3.65 \mu\text{m}$) was
61 mainly found in the lower cloud layer. On the other hand, the mode 2 ($\bar{r} = 1.0 \mu\text{m}$) and mode
62 2' ($\bar{r} = 1.4 \mu\text{m}$) number densities dispersing throughout the main cloud deck, peaking in the
63 lower clouds but in slightly different altitude regions (Ragent et al., 1985). The diffusional
64 growth of mode 2 and mode 2' particles from sulfuric acid vapors can be transported
65 downwards into the lower part of the cloud deck by eddy diffusion (Imamura and Hashimoto.,
66 1998; McGouldrick., 2017). The lower clouds can be probed using the CO₂ atmospheric
67 window in near-infrared (NIR) regime (Allen & Crawford, 1984). Akatsuki's IR2 camera has

68 three filters (1.735 μm , 2.26 μm , and 2.32 μm) to observe the lower clouds in Venus's nightside
69 (Sato et al., 2016). Contrast features emerging in these filters are due to spatially
70 inhomogeneous scattering and absorption of the radiation from the lower atmosphere by cloud
71 particles. Until now, the morphology studies have been performed by using image enhancing
72 techniques to identify interesting features (Peralta et al., 2019, Horinouchi et al., 2017).
73 However, accurate photometric studies have never been performed due to data contamination
74 by dayside light until the development of imagery restoration methods: 'Restoration by Simple
75 Subtraction' (Sato et al., submitted) and 'Restoration by Deconvolution' (this paper). Also,
76 the aerosol properties can be investigated utilizing different filters in IR2 (2.26 μm and
77 1.735 μm) such as analyses done on observations by Galileo Near Infrared Mapping
78 Spectrometer (NIMS) during Venus flyby and Visible and Infrared Thermal Imaging
79 Spectrometer (VIRTIS) on board Venus Express (VEx) to evaluate aerosol size distributions
80 using 2.30 μm and 1.74 μm infrared radiations (Carlson et al., 1993; Wilson et al., 2008).

81

82 Venus is dominated by a global atmospheric circulation known as the super-rotation (Schubert,
83 1983). In contrast to the slow rotating planet body (1.6 m/s westward), the wind speed can
84 reach up to ~100 m/s near the cloud top (~ 70 km altitude) whereas it slows down to ~70m/s
85 in the lower clouds z~50km (Carlson et al., 1991; Hueso et al., 2012). In the observations by
86 Akatsuki, there have been reports of the occurrence of 'dark-markings' or 'discontinuity'
87 features (Peralta et al., submitted). These 'discontinuity' features can be described as a sharp
88 change in the cloud opacity that results in distinct boundaries in observed transmission of
89 clouds propagating westwards. Peralta et al. (submitted) suggested that the 'discontinuity'
90 features can propagate at speeds of ~90 m/s. Amongst these findings, two events on Aug-18
91 and Aug-27 were the largest discontinuity features observed by Akatsuki are also termed as
92 'Enormous Cloud Cover' (ECC) in this paper. At present, there have been dynamical studies

93 suggesting mechanisms making the ECC feature could be manifestation of Kelvin waves
94 (Peralta et al., submitted). However, the actual compositions of aerosols were not well known
95 due to the light contamination over the IR2 nightside data. This becomes the main motivation
96 for the purpose of this paper to supply accurate photometric evidences utilizing enhanced RD
97 processed images.

98

99 Satoh et al., (submitted) has improved data qualities of Akatsuki/IR2 by developing the
100 ‘Restoration by Simple Subtraction’ (RSS) method which separates the nightside emission
101 features from the strong contamination due to spread of dayside light. This has enabled quality
102 photometric studies for the first time ever. However, the RSS method is unable to restore light
103 spreading property of the nightside photometry by the IR2 camera’s PSF. This leads to the
104 scope of this paper to further improve the photometric accuracy by true contrast level using
105 deconvolution technique in ‘Restoration by Deconvolution’ (RD) method.

106

107 The main outline of this paper would begin with data selection for restoration targets and
108 photometric analyses (Section 2), introducing the development of RD method (Section 3),
109 evaluating aerosol properties of the ECC (Section 4), and finally to discuss the possible
110 interpretations of the ECC’s microphysical properties (Section 5).

111

112 **2. Data**

113 **2.1. IR2 data**

114 The IR2 camera onboard Akatsuki utilizes narrow band filters in the atmospheric windows to
115 probe through the middle and lower clouds of Venus atmospheric windows (Satoh et al., 2016).

116 The three filters of the IR2 camera used to observe the nightside are 1.735 μm , 2.26 μm , and
117 2.32 μm . Infrared radiation originating from lower altitudes are attenuated by CO₂ absorption

118 in 1.735 μ m and 2.26 μ m, whilst 2.32 μ m contains CO absorption band. To save downlink time
119 from Akatsuki, ‘Region of Interest’ (ROI) function of the onboard computer trims the image
120 frame of 1024 x 1024 pixels (thereinafter denoted as ‘1k-frame’) into smaller pixel frame size
121 [X1:X2, Y1:Y2] focusing only on region for Venus disk observations. The IR2 camera is
122 operated under cooling temperature of the platinum silicide (PtSi) detector regulated by the
123 cryocooler to be below 70K. This is crucial to Venus nightside observations because the
124 thermally induced electrons saturate the detector within few tens of seconds when the detector
125 temperature is 70K (Sato et al., 2016).

126

127 The data used in this paper (Table 1a and 1b for 2.26 μ m and 1.735 μ m filters respectively) are
128 L2B data available from “Akatsuki 2- μ m Camera (IR2) Data Archive” on Data Archives and
129 Transmission System (DARTS) (Murakami et al., 2018). L2B data are observations by IR2
130 camera in 1.735 μ m, 2.26 μ m, and 2.32 μ m filters. L2B data for the three filters experience data
131 contamination by the camera’s PSF and intense dayside crescent and pixel saturation when the
132 number of photoelectrons exceeds the upper limit of the pixel’s potential well (Examples
133 shown in Figure 1). The overall output of L2B images appears to have a dependency on
134 operating temperature. This is described as temperature-dependent sensitivity of IR2 and the
135 data were corrected using functions described in Sato et al. (submitted). The correction for
136 geographic mapping was conducted by improved image navigation maximizing the radial
137 (inward) component of the gradient of radiance (Horinouchi et al., 2017).

138

139 We have selected data from orbit 24 and 25 having wide spatial and temporal coverage on
140 Venus nightside observations. However, we focus especially on the data of dates Aug-18 (from
141 orbit 24) and Aug-27 (from orbit 25). The main reason to this is to focus observations on the
142 ‘Enormous Cloud Cover’ (ECC) features. Data from these two dates during apoapsis passage

143 observing Venus are ideal for investigating daylight spreading by point spread function (PSF)
144 while high resolution nightside observations are as frequent as 2-hours intervals. Note that L2B
145 images from these observations were trimmed by the ROI function i.e. [129:896, 385:1024].

146 [Table 1]

147 [Figure 1]

148 **3. Methodology**

149 The condition for deconvolution process requires the saturated pixels being estimated in L2B
150 under all possible factors influencing the IR2 observations. Then, deconvolution by model-
151 PSF can be performed on the entire observing frame. Thus, the steps (Figure 2a) to preparing
152 for the Restoration-by-Deconvolution (RD) are: Step 1. Modelling Point Spread Function
153 (PSF); Step 2. Modeling dayside and nightside radiances using radiative transfer; Step 3.
154 ‘Model Venus Disk’ (Dayside + Nightside) convolved by model-PSF; Step 4. Saturated pixels
155 in L2B replaced by ‘Convolved Model’ from (Step 3); Step 5. (Step 4) undergoes
156 Deconvolution by model-PSF. The sequential image preparations from Step 1 to Step 5 are
157 summarized in Figure 2b.

158 [Table 2]

159 [Figure 2]

160

161 **3.1. Modelling the IR2 Point Spread Function (PSF)**

162 We modified the mathematical approximation introduced by Satoh et al. (2017) that initially
163 incorporates both point-symmetric and axisymmetric terms to include an additional diffusive
164 term. The current PSF reported in this paper also incorporates updated parameters for
165 approximating both the point-symmetric and axisymmetric terms.

166

167 The three components of the PSF model are: a point-symmetric term [$a_r(r)$] and two
 168 axisymmetric terms [$a_x(X)$ and $a_y(Y)$] from Satoh et al. 2017; and a newly introduced
 169 diffusive term $d(X, Y)$.

$$\text{PSF}(X, Y) = g_1 a_r(r) + g_2 a_x(X) \times a_y(Y) + d(X, Y) \quad (1)$$

170 where

$$r^2 = X^2 + Y^2$$

$$X = x - x_0$$

$$Y = y - y_0$$

174 where (x_0, y_0) is the center of the PSF.

175 The point symmetric term $a_r(r)$, and axisymmetric terms $a_x(X)$ and $a_y(Y)$ are expressed as
 176 the following (Satoh et al., 2017):

$$a_r(r) = \frac{\Gamma_1}{2\pi \left[r^2 + \left(\Gamma_1/2 \right)^2 \right]^{e_1}} \quad (2)$$

$$a_x(X) = \frac{\Gamma_2}{2\pi \left[X^2 + \left(\Gamma_2/2 \right)^2 \right]^{e_2}} \quad (3)$$

$$a_y(Y) = \frac{\Gamma_2}{2\pi \left[Y^2 + \left(\Gamma_2/2 \right)^2 \right]^{e_2 c}} \quad (4)$$

177 where the parameters were updated as the following:

Γ_1	0.30	e_1	1.18	g_1	3.30
Γ_2	8.0	e_2	0.83	c	1.30

178

179 In the latest version of PSF modelling, the region within the first halation ring is a ‘hole’ in the
 180 axisymmetric term. This is to simulate the perfect internal reflection during first point of
 181 contact of remnant light in the PtSi substrate. In addition, we incorporate another diffusive term

182 d(X, Y) to that spreads further away from the intensive light source. This may be due to light
183 reflections that results in out-focused ‘ghosts’ of the bright object.

184 The diffusive term d(X, Y) is defined as follow:

$$d(X, Y) = 1.4 \times 10^{-6} \times \exp \left[- \left(\frac{r}{400} \right)^2 \right] \quad (5)$$

185 The closeness of our model-PSF can be compared with the light spreading properties in L2B
186 data. We selected 2.02 μ m L2B data from orbit 14, 15, and 16 (dayside observations) below
187 45° phase angle to analyze the PSF properties. In each observation, the Venus disk is being
188 masked to measure the total amount of flux outside the disk (termed as ‘Loss to off-disk flux’).
189 The ratio of ‘Loss to off-disk flux’ to ‘total flux’ is being plotted against the spacecraft distance
190 from Venus (Figure 3). Similarly, we take same measurements for our model PSF-convolved
191 dayside (where optical fogging was also included). Light spreading properties by our model-
192 PSF were found to match well to those of the observations as illustrated in Figure 3.

193

194 [Figure 3]

195

196 **3.2. Radiative transfer calculation**

197 **3.2.1. Discrete ordinate radiative transfer for nightside emission**

198 The Radiative Transfer computation incorporates “discrete ordinate RT” developed by
199 Stamnes et al. (1988) combining with the line-by-line radiative transfer to calculate
200 transmittance spectra for sub-layers of Venus atmosphere. The computation treats Venus
201 atmospheres as stacked layers each of which is 2-km thick. Each layer was assumed to be
202 homogeneous in temperature, pressure, and molecular and aerosol compositions. Then, the
203 atmospheric Pressure-Temperature profile (2-km resolution) was obtained from observations
204 by PV probe by Seiff (1982). The molecular lines implemented were obtained from ‘High-
205 resolution Transmission’ (HITRAN) molecular absorption database for CO₂, N₂, CO, H₂O, and

206 HCl. Also, the radiative transfer calculation assumes the aerosols are droplets of 85% H₂SO₄
 207 aqueous solution (Palmer & Williams, 1975), and the size-distribution parameters were
 208 extracted from Grinspoon et al. (1993). Whereas, absorptions by continuum were set as
 209 $5.6 \times 10^{-9} \text{ cm}^{-1} \text{ amagat}^2$ at 1.735 μm and $3.5 \times 10^{-8} \text{ cm}^{-1} \text{ amagat}^2$ at 2.26 μm .

210

211 The nominal cloud model incorporates the particle mode distributions locating at different
 212 altitudes within the middle and lower clouds where absorptions above 62km were neglected:
 213 $z=48\text{-}52\text{km}$ (mode 3, $\tau=14$); $z=52\text{-}54\text{km}$ (mode 2', $\tau=14$); $z=56\text{-}60\text{km}$ (mode 2, $\tau=5$); $z=60\text{-}$
 214 62km (mode 1, $\tau=2$). This trimodal distribution is summarised in Table 3a and extinction cross
 215 sections are summarised in Table 3b. The limb darkening equations attained from the radiative
 216 transfer are presented as follow (Sato et al., submitted):

217

$$I'_{1.735\mu\text{m}} = \frac{I_{1.735\mu\text{m}}}{0.6423 \cos(\theta_{\text{em}}) + 0.3577} \quad (6)$$

218

$$I'_{2.26\mu\text{m}} = \frac{I_{2.26\mu\text{m}}}{0.6904 \cos(\theta_{\text{em}}) + 0.3096} \quad (7)$$

219 where I' is limb-darkening corrected intensity, I is observed intensity, and θ_{em} is emission
 220 angle.

221 [Table 3a]

222 [Table 3b]

223

224 3.2.2. Preparation for 'Model Dayside' (MDD)

225 The calculation for dayside reflectance was referred to the line-by-line radiative transfer by
 226 Sato et al. (2020) developed for modeling 2.02 μm dayside intensities. This model was
 227 translated for calculating dayside intensities in both 2.26 μm and 1.735 μm filters to generate

228 dayside models $MDD_{2.26\mu m}$ (Model Dayside Disk in $2.26\mu m$) and $MDD_{1.735\mu m}$ (Model
229 Dayside Disk in $1.735\mu m$). The dayside photometry calculated by radiative transfer accounts
230 for the nominal cloud model from Haus et al. (2015). Considering possible intrinsic changes
231 of spatial and temporal variations of Venus clouds from one image to another, we have to
232 introduce a factor so-called ‘Dayside F factor’ (denoted as F) to adjust the dayside intensities
233 based on observation conditions of every image (Appendix A).

234

235 **3.3. Preparation for ‘Cleaned Nightside’ (CLN)**

236 For $2.26\mu m$, ‘Cleaned Nightside’ $CLN_{2.26\mu m}$ was adapted from RSS-processed images (Satoh
237 et al., submitted). After acquiring ‘Restoration-by-Deconvolution Data’ ($RDD_{2.26\mu m}$),
238 $RDD_{2.26\mu m}$ can be used as a baseline to model $CLN_{1.735\mu m}$. Both $2.26\mu m$ and $1.735\mu m$ being
239 in the windows of the CO_2 atmosphere have slightly different contrast and photometric
240 emissions due to the differences in scattering properties by aerosols. $CLN_{1.735\mu m}$ can be
241 estimated from $RDD_{2.26\mu m}$ based on the conversion relationship described by emission
242 properties in the two filters ($1.735\mu m$ and $2.26\mu m$) as calculated by radiative transfer in
243 Equation 8 (Satoh et al., submitted)

$$\text{Log}(CLN_{1.735\mu m}) = m \times \text{Log}(RDD_{2.26\mu m}) - 0.157 \quad (8)$$

244 where $m=0.598$ is the conversion factor estimated by radiative transfer.

245

246 **3.4. Preparation for Deconvolution by PSF in RD-method: RDD**

247 As the observations suffer saturation when the capacity of each pixel is overflowed, both
248 photometry in saturated region and outside the ROI frame were lost. Thus, we have to model
249 the loss photometry to prepare the data for deconvolution process.

250

251 Deconvolution requires all light spreading as much as possible to ‘re-absorb’ the photometry
252 extended by the long PSF tail back to its light source. Hence, we prepare a larger 2048 x 2048
253 pixels² size canvas (denoted as ‘2k-frame’) to accommodate model photometry estimation
254 outside the ROI frame. The data used in this paper for Aug-18 and Aug-27 were trimmed by
255 [129:896, 385:1024] in the ROI function. The observing CCD’s 1k-frame is fixed into the
256 middle of the prepared 2k-frame where light spreading by PSF outside the ROI frame can be
257 accommodated. The use of larger canvas can also suppress repetition of artifacts when inverse
258 Fourier transform of the entire frame is being applied in deconvolution.

259

260 ‘Model Dayside Disk’ (MDD) (from Section 3.2.2) and ‘Cleaned Nightside’ (CLN) (from
261 Section 3.3) together make up the full ‘Model Day + Nightside’ (MDN). The MDN can then
262 be convolved by model-PSF giving ‘Convolved Model’ (CVM) where saturated pixels in L2B
263 and the canvas vessel outside the ROI frame (2k-frame) can be replaced to estimate loss
264 photometry (Figure 4-right).

265

266 In this process, only saturated pixels were being replaced making up the ‘Combined-image’
267 (COM) while keeping unsaturated pixels unchanged. Now, this suffices the condition for RD-
268 method requiring the saturated pixels to be appropriately determined where deconvolution by
269 model-PSF can be performed on the entire frame (COM).

270

271 [Figure 4]

272

273 **3.5. Calibration for optical Fogging**

274 In typical L2B observations, there are ‘ghost-features’ due to light remnants bouncing off the
275 glass surfaces in the IR2 camera optics. Thus, this gives an overall offset photometry to the

276 nightside observations. This offset radiance (also termed as ‘fogging’) is hence dependent on
 277 the total incoming flux in which is also dependent on both phase angle and apparent diameter.
 278 The fogging amount is summarized in Table 4 where they do not have significant influence in
 279 both 2.26 μm and 1.735 μm filters. Refer to Figure 7 and 8 showing the upper limit of fogging
 280 influence when fogging amount is multiplied by 10. The original L2B unsaturated pixels can
 281 be subtracted by fogging value for each observation (Table 4) before the replacement for
 282 saturated pixels (giving COM) to suppress this minimal offset by fogging: $L2B' = L2B - \text{Fog}$
 283 where L2B' is corrected L2B, and Fog is ‘Fogging value’ obtained from Table 4.

284

285 [Table 4]

286

287 **4. Results**

288 **4.1 Restoration by Deconvolution (RD) with Richardson-Lucy Algorithm**

289 The deconvolution incorporated in the RD-method utilizes the Richardson-Lucy (R-L)
 290 Algorithm (Lucy., 1974) which is an iterative computation that restores underlying pixels that
 291 has been contaminated by the PSF. Assuming we have an observed image that is expressed as:

$$I(X, Y) = \iint_{-\infty}^{\infty} [I_0(X, Y) \times \text{PSF}(X, Y) dXdY] + \delta(X, Y) \quad (9)$$

292

293 where $I(X, Y)$ is the observed image, $I_0(X, Y)$ is the ideal image, $\text{PSF}(X, Y)$ is our model-PSF
 294 (from Equation 1), and $\delta(X, Y)$ is random noise associated to the observed image. Equation 9
 295 can also be simplified as:

$$I(X, Y) = I_0(X, Y) * \text{PSF}(X, Y) + \delta(X, Y) \quad (10)$$

296 where ‘*’ means convolution in the Fourier transform space.

297 The R-L deconvolution algorithm can then be expressed as the following:

$$I_{n+1}(X, Y) = I_n(X, Y) \left(\frac{I_0(X, Y)}{I_n(X, Y) * \text{PSF}(X, Y)} \right) * \text{PSF}'(X', Y') \quad (11)$$

298

299 where n is number of iterations, $I_{n+1}(X, Y)$ is output image from each iteration, and
 300 $\text{PSF}'(X', Y')$ is PSF in inverse Fourier transform space

301

302 In each iteration of the R-L algorithm (Equation 11), the output image (I_{n+1}) is estimated
 303 restored image array fitting $I_{n+1}(X, Y)$ more closely to $I_0(X, Y)$ than the previous n^{th} iterations
 304 i.e. $I_{n+1}(X, Y) \rightarrow I_0(X, Y)$. To test which number of iterations (n) is best for our RD-method,
 305 we experiment R-L algorithm with known answer image (I_0) and known PSF-model while
 306 monitoring the standard deviation (SD) of the resultant image (I_{n+1}) to I_0 in every iteration (not
 307 shown). It was found that $n \geq 40$ is sufficient to stabilize the $I_{n+1}(X, Y) \rightarrow I_0(X, Y)$ at SD of
 308 ~ 0.01 . Hence, we consistently apply $n=50$ for R-L deconvolution in our RD-method.

309

310 **4.2. Photometric analysis on the Enormous Cloud Cover using RDD images**

311 In orbits 24 and 25, two largest events of the discontinuity features (ECC) up to latitudinal
 312 extent of $\sim 30^\circ$ North to $\sim 40^\circ$ South (Peralta et al., submitted) have been observed by Akatsuki
 313 on 2016 Aug-18 and Aug-27 data. The restoration processes have made these observations
 314 more evident for accurate photometric analysis of these events initiating from near the
 315 terminator (See Figure 5).

316 [Figure 5]

317

318 The transmittance of the ECC can be measured as follow:

$$\text{TR} = \frac{I_{\text{ECC}}}{I_{\text{BC}}} \quad (12)$$

319

320 where I_{ECC} is the intensity in the darker ‘Enormous Cloud Cover’ (ECC), and I_{BC} is the
321 brighter ‘Background Clouds’ (BC).

322

323 The region selection for photometric measurements is taken at low latitudes (-5° to 5°). I_{ECC}
324 and I_{BC} are average radiance of 10° longitude x 10° latitude square ‘box’ shaped regions
325 (thereinafter denoted as ‘10x10-region’) each positioned in the optically thick ECC and
326 optically thin BC regions respectively (Figure 6). They were set to be 10° longitudinal distances
327 apart while tracking along the propagation of the ECC discontinuity front in subsequent 2 hours
328 interval images. The box regions were shifted longitudinally according to the estimated
329 propagation speed of the ECC $\sim 90\text{m/s}$ (Peralta et al., submitted). The measurements for I_{ECC}
330 and I_{BC} are summarised in Table 5. The averaged radiance measurements obtained from the
331 respective 10x10-regions for I_{ECC} and I_{BC} show stable emissions of the ECC emerging from
332 near the terminator traveling further into the west. This demonstrates the ability of RD process
333 to revert light spreading contamination from the dayside at regions near the terminator. Then,
334 the measurements for all observations as time evolution are plotted in Figure 7 and Figure 8
335 for Aug-18 and Aug-27 respectively where upper limits of Fogging (Fogging value from Table
336 4 multiplied by 10) are also being illustrated. To avoid uncertainties in regions too close to the
337 terminator or limb, we select observations of the ECC feature within the region of incident
338 angle $> 130^\circ$ and emission angle $< 75^\circ$ for photometric analyses. The discussion on
339 uncertainties associated to the region selection will be further discussed in Section 5.1.

340

341 [Table 5]

342 [Figure 6]

343 [Figure 7]

344 [Figure 8]

345

346 **4.3. Interpretations on aerosol properties of the Enormous Clouds (ECC)**

347 The radiative transfer computation as explained in Section 3.2. calculates the wavelength-
348 dependent (1.735 μm and 2.26 μm) theoretical transmittance (attenuation) by an additional layer
349 of single-mode aerosols (mode 1, mode 2, mode 2', and mode 3) between 54 to 56 km altitudes.
350 Extinction cross sections (k_{ext}) incorporated are obtained from the computation for Mie
351 scattering (summarised in Table 3b). For 2.26 μm , the relationship between the additional
352 optical thickness (τ) by different aerosol modes and observed transmittance (TR) can be
353 expressed as the following:

$$\begin{aligned} \tau = & -A3(\log(\text{TR}_{2.26\mu\text{m}}^{\text{obs}}))^3 - A2 \times (\log(\text{TR}_{2.26\mu\text{m}}^{\text{obs}}))^2 \\ & - A1 \times \log(\text{TR}_{2.26\mu\text{m}}^{\text{obs}}) - A0 \end{aligned} \quad (13)$$

354 where τ is optical depth and $\text{TR}_{2.26\mu\text{m}}^{\text{obs}}$ is observed transmittance in 2.26 μm , and the constants
355 ($A0$, $A1$, $A2$, and $A3$) for different particle size modes are summarised in Table 6 whereas the
356 optical thickness τ for 1.735 μm measurements can then be computed by multiplying
357 $\tau(2.26\mu\text{m})$ by the ratio of extinction cross sections in Table 3b.

358

359 [Table 6]

360

361 The relationships of the theoretical transmissions to the optical depths for different particle
362 modes (mode 1, mode 2, mode 2', and mode 3) are portrayed in Figure 9. Using Equation 13,
363 the optical thicknesses calculated from the measurements ($\text{TR}_{2.26\mu\text{m}}^{\text{obs}}$) obtained from respective
364 10x10-regions (Table 5) for each observation are summarised in Table 7.

365

366 [Figure 9]

367

[Table 7]

368

369 The optical thickness (τ) obtained together with the extinction cross sections (Table 3b) as
370 calculated from Mie computations for both filters can be used to calculate the column density
371 of particles (N) (summarised in Table 8a). The total column mass of the H_2SO_4 droplets can
372 then be calculated (summarised in Table 8b) from $M = N \times m$ (M is total column mass) where
373 $m = \rho V$ where ρ is 1.834 g cm^{-3} and V is spherical volume of sulphuric acid droplets where
374 particle size mode's \bar{r} can be referred to Table 3a.

375

376

[Table 8]

377

378 Figure 10 portrays transmissions measured in the observations (08-18/15:33 to 21:33; 08-
379 27/20:03 to 22:03) over the theoretical transmission curves (mode 1, mode 2, mode2', and
380 mode 3). The observational points for averaged transmissions include error bars that account
381 for spatial variabilities within the measured 10×10 -region. Clearly the range of measurements
382 shows that mode 1 cannot be accounted for possible aerosol mode candidate of the ECC. Hence,
383 consideration for mode 1 particles can be exempted from here. This leaves us the possibilities
384 for mode 2, mode 2', and mode 3 to be accounted for the composition of the ECC.

385

386 If considering attenuation by additional layer of mode 2, the overall optical thicknesses of all
387 observations (08-18/15:33 to 21:33; 08-27/20:03 to 22:03) are in the range of $\tau_{2.26\mu\text{m}} \sim 11.4$ -
388 26.7 in $2.26\mu\text{m}$ (where $\tau_{1.735\mu\text{m}}$ is 1.385 times larger by referring to wavelength dependent
389 extinction cross section in Table 3b). This means column densities of ~ 1.3 - 3.0 ($\times 10^8$ particles
390 per cm^2) amounting to column masses of ~ 1.0 - 2.3 (mg per cm^2) are required to suffice the
391 observed additional opacity.

392

393 Then, consideration of mode 2' gives optical thicknesses range of $\tau_{2.26\mu\text{m}} \sim 12.3-28.8$ in
394 $2.26\mu\text{m}$ (where $\tau_{1.735\mu\text{m}}$ is 1.08 times larger). This results to column densities of $\sim 5.5-12.7$
395 ($\times 10^7$ particles per cm^2) amounting to column masses of $1.2-2.7$ (mg per cm^2) are required to
396 suffice the additional optical depths.

397

398 Finally, consideration of mode 3 gives optical thicknesses range of $\tau_{2.26\mu\text{m}} \sim 5.3-11.3$ in
399 $2.26\mu\text{m}$ (where $\tau_{1.735\mu\text{m}}$ is 1.023 times larger). This leads to column densities of $\sim 4.8-10.3$
400 ($\times 10^6$ particles per cm^2) amounting to column masses of $1.8-3.9$ (mg per cm^2) are required to
401 suffice the additional optical depths. Be reminded that these value ranges estimated here are
402 taken from the extreme measurements (lower and upper limits) where the mode value is
403 somewhere within the range for each observation.

404

405 Regardless of particles size, interesting point to note here is that the required amount of column
406 masses to cause the observed optical thicknesses in particles modes (mode 2, mode 2' and
407 mode 3) are not so different. The same amount of sulfuric vapor can condense into particles
408 mode 2, mode 2' and mode 3 to reproduce the observed TR of the ECC. Therefore, all three
409 particles modes (mode 2, mode 2', and mode 3) are possible candidates for constituting of the
410 ECC layer at the current analysis stage. Also, we have to acknowledge that the measurements
411 obtained from the corresponding 10×10 -regions in each observation averaged out the spatial
412 variations within each choice of area. This inspired us to continue explore at finer region
413 resolution of 4° longitude x 4° latitude box region (thereinafter denoted as '4x4-region') for
414 spatial variabilities in each measurement.

415

416

[Figure 10]

417

418 **5. Discussions**

419 **5.1. Accuracy of RD method**

420 We evaluate the accuracy of our RD-method by comparing the closeness of our results to the
421 L2B data. We perform this by re-convolving our resultant RDD by model-PSF (denoted as
422 ‘Convolved-RD’ = CRD), and to compare its deviation to the original L2B. The deviation is
423 given by the following equation:

$$SD = \sqrt{\frac{\sum |CRD - L2B|^2}{N}} \quad (14)$$

424 The ‘SD’ measures the standard deviation for CRD to L2B (in units of $W m^{-2} sr^{-1} \mu m^{-1}$), and
425 hence estimating the deviation of our RD-method and PSF to L2B original data. We obtain the
426 SD measurements in bins of 10° incident angles while plotting it by incident angles away from
427 the terminator (incident angle = 90°).

428

429 The plot (Figure 11) shows larger SD values near the terminator indicating some level of
430 influence by dayside still remains in both $2.26\mu m$ and $1.735\mu m$. The trend shows a rapid
431 decrease until it starts to stabilize from about 130° incident angles and above at SD of $\sim 0.001-$
432 $0.003 Wm^{-2}sr^{-1}\mu m^{-1}$ in $2.26\mu m$ and $\sim 0.003-0.0035 Wm^{-2}sr^{-1}\mu m^{-1}$ in $1.735\mu m$. Thus, we
433 perform photometric analysis for regions above 130° incident angles for better photometric
434 accuracies (defined as ‘photometrically stable region’). The small SD in photometrically stable
435 region demonstrates the fidelity of RD-process is good to the observed L2B images. To remark,
436 the SD estimation includes uncertainties associated to various properties: PSF model, plane
437 parallel approximation in radiative transfer for calculating dayside reflectance, and fogging
438 estimation.

439

440

[Figure 11]

441

442 **5.2. Identity of the Enormous Cloud Cover (ECC)**

443 According to the interpretation from Figure 10 (Section 4.3), there is no definitive conclusion
444 of exactly which particle modes are composited in the ECC. However, if assuming ECC is of
445 only mode 3 particles, the Aug-18 event would consist of number density of $\sim 5.2-9.2$ ($\times 10^6$
446 particles per cm^2) which is within the range to that of Aug-27 event giving number density of
447 $\sim 4.8-10.3$ ($\times 10^6$ particles per cm^2). This could imply that both events are akin to each other
448 given the similar physical properties.

449

450 We would like to focus on discussing the data point of 08-18/15:33 that lies almost exactly on
451 the mode 3 theoretical curve. To further the investigation, we use finer 4x4-regions to probe
452 for spatial variabilities within the 10x10-region. To specify, 1° longitude unit and 1° latitude
453 unit on Venus both corresponds to ~ 106 km distance. Therefore, 10x10-region and 4x4-region
454 are 1060km x 1060km and 424km x 424km respectively on Venus geographical coordinates.
455 The original 10x10-region averages the radiance (hence transmission) value within the area
456 selected which may be missing out detailed transmittance level by finer regions. Bear in mind
457 that the measurements for I_{ECC} and I_{BC} obtained for regions in ECC and background cloud
458 (BC) are from separated regions (10° longitudinal distance apart i.e. 1060km apart). This means
459 that to account for all possible spatial variabilities, the transmission measurements have to be
460 all possible combinations of I_{ECC} and I_{BC} ($\text{TR} = I_{\text{ECC}}/I_{\text{BC}}$). Thus, our 4x4-regions scanning
461 within the 10x10-region for both I_{ECC} and I_{BC} also have to be of all combinations. The key
462 point of incorporating such combinations is because the underlying cloud conditions are
463 unknown and may be changing spatially. Therefore, this motivates our study to be extended
464 into a statistical one to explore all possibilities of aerosol distributions in the ECC.

465 To do so, we start by moving the 4x4-region across 10x10-region on each side (latitudinally or
466 longitudinally) for which there can be 6° shifts resulting in 7 different positions. This gives us
467 a total of 49 different positions when scanning thoroughly in each 10x10-region selected for
468 the ECC and BC respectively. Then, each I_{ECC} and I_{BC} measured from 4x4-region would have
469 49 positions each that gives a total of 2401 possible combinations for $TR = I_{ECC}/I_{BC}$.

470

471 Interestingly, the scatter plots of ‘TR ratios by 4x4-region’ (thereinafter denoted as ‘TR4’)
472 indicate near-parallel alignment to the theoretical transmittance curves regardless of the choice
473 of combinations (Figure 12). This implies the robustness of our method to infer particle
474 modes/sizes by comparing observed transmittance to the theoretical curves. TR4 scattering
475 along the theoretical curve can be related to the variability of optical thicknesses where towards
476 upper right end is more optically thin and towards lower left is more optically thick. On the
477 other hand, the deviation from parallel-ness to the mode 3 theoretical curve is affected by the
478 selection of respective I_{ECC} and I_{BC} measurements from 4x4-region where the deviation is
479 indicative of non-mode 3 trend of either the ECC or BC. The slight deviation from parallel
480 alignment to the theoretical curves can be interpreted as two possible contributions: 1. Cause
481 of varying transmissions in the ECC (can be interpreted from I_{ECC} statistics); 2. Cause of
482 varying opacities in the BC (can be interpreted from I_{BC} statistics).

483

484 The scatters are encompassing well along the mode 3 curve and with small fraction of points
485 touching the mode 2’ theoretical curve. Thus, this can be interpreted as the ECC is composite
486 of mostly mode 3 where possible fractional mixings of smaller particles may be considered.

487

488

[Figure 12]

489

490 5.3. Characterizing the background cloud (BC)

491 To characterize the BC, we consider two categories (with two sub-groups) of the statistical
492 scatter plot by 4x4-regions in Figure 12. To lower the TR4 data points ‘Case-L’ (L means Low
493 TR4): we need either brighter I_{BC} than ‘normal’ radiances ‘Case-LBC’ (subscript of ‘BC’ means
494 lower/higher TR4 by manipulating BC); or darker I_{ECC} than normal intensity ‘Case-LECC’. In
495 contrast, to increase the data points towards higher TR4 ‘Case-H’ (H means High TR4): we
496 need either darker I_{BC} than normal radiances ‘Case-HBC’; or brighter I_{ECC} than normal ‘Case-
497 HECC’. ‘Normal’ value range here is defined as data points within the standard deviations ($f =$
498 0.8 where half of the data points lies) of the mean value for the I_{BC} and I_{ECC} statistics. To note
499 that by manipulating I_{BC} or I_{ECC} statistics, we can relate them to where their transmission
500 distribution lies on the plot for the BC or ECC respectively. These two cases (of two sub-groups
501 respectively) are summarized in Table 9a-b.

502

503 [Table 9a]

504 [Table 9b]

505

506 We consider extreme cases of I_{BC} data points being brighter than ‘normal’ (Case-LBC), and I_{BC}
507 is darker than normal (Case-HBC). Despite the extremity of the selections, both Case-LBC
508 (Figure 13a) and Case-HBC (Figure 13b) align well along the mode 3 theoretical curve. Possible
509 explanation is that the lower cloud layer is constantly being heated by infrared radiation
510 originating from the hot lower atmosphere and the ground. The radiation is being absorbed by
511 the cloud particles which drives convection here (Imamura et al.2014; Baker et al., 1998). This
512 process activating the growth of particles into larger size occurs throughout the background
513 cloud. Thus, spatial variations in the BC are almost constantly mode 3 throughout the bright
514 and dark radiances which is being suggested by the statistical analysis.

515

516 To compare, we now perform the opposite experiment to evaluate the extreme cases of I_{ECC}
517 data points being darker than ‘normal’ (Case-LECC), and I_{ECC} is brighter than normal (Case-
518 HECC). Extreme Case-LECC shows the scatter points (red) grouping slightly underneath the
519 mode 3 curve (Figure 13a). In contrast, the extreme Case-HECC illustrates scatter points (red)
520 grouping above the mode 3 curve (Figure 13b). While the preceding Case-LECC can still be
521 related to mode 3 with possible mixing of smaller mode particles, the latter Case-HECC is
522 beyond the coverage by mode 3 theoretical curve. This opens the discussions to other
523 considerations to be taken into account to relate to those data points over the theoretical curve
524 range (Case-HECC).

525

526 [Figure 13]

527

528 **5.4. Different approaches to explain observed transmissions**

529 **5.4.1. Approach 1: Alternative mode 3 size distributions (Mode 3’)**

530 Here, we consider transmittance by single-mode aerosols with mean radius varied from mode
531 3 (named mode 3’): from $2.0\mu\text{m}$ to $4.50\mu\text{m}$ in $0.25\mu\text{m}$ intervals. For clarity reason, we show
532 in Figure 14 only the theoretical curves for intervals of $0.5\mu\text{m}$ to avoid crowding the plots in
533 minimal range. The transmittance scatter plots of 08-18/15:33 are in two groups on the
534 transmission correlation plot. The LECC are grouped on the mode 3’ ($\bar{r}=2.00\mu\text{m}$) curve whereas
535 the HECC are still above all mode 3’ curves considered.

536

537 Even by modifying the width of size distribution of standard mode 3 particles to be one fifth
538 of the original (uppermost curve) cannot explain the HECC data points. Thus, although some of

539 the transmittance scatter points coincide with a part of mode 3' curves, this approach still
540 cannot explain those beyond the mode 3 alternatives' theoretical curves.

541

542 [Figure 14]

543

544 **5.4.2. Approach 2: Consideration for different altitude levels of the ECC's aerosols**

545 Then, we consider for different altitude elevations for transmissions by single-mode aerosols
546 of mode 3 in the ECC. The original radiative transfer computation assumed an additional layer
547 of single-mode aerosols at the altitude range $z=54-56\text{km}$ (Figure 10). We vary the radiative
548 transfer calculations for emissions by single-mode aerosols (only mode 3 for this study) at
549 different altitudes varying from 48-60km (at 2km intervals). The theoretical curves for varying
550 altitudes ($z=48-60\text{km}$) are being expressed in Figure 15 with scatter plot (for all TR4
551 combinations) overlying the curves. Fascinatingly, the scatter plot fits well within the
552 theoretical curves between altitudes at $z=50\text{km}$ (bottom line) and $z=60\text{km}$ (upper line). This
553 suggests consideration for varying altitudes is a promising candidate for further interpretations
554 of the data.

555

556 [Figure 15]

557

558 The other interesting thing we can benefit from our statistical analysis is to interpret the
559 distribution probabilities of particles at different altitudes across any region of selection within
560 the ECC. In Figure 16 a-c, we show statistical distribution of I_{ECC} starting from constant
561 longitudinal region closest to the discontinuity front shifting across 1° longitudinal distance
562 away from the front every measurement. These groups of measurements are denoted as 'LO_n'
563 where 'LO' comes from 'Longitude' and 'n' is number of constant longitudes $^\circ$ away from the

564 first one 'LO_0'. LO_0 is the closest distance (~424 km from the front) to the discontinuity
565 front for I_{ECC} and furthest for I_{BC} . To note, LO_0 is set to be about 4° longitudinal distance
566 behind the exact front to avoid uncertainties associated to the estimated speed of 90m/s while
567 tracking the ECC front feature (Figure18). Then, +1° longitude shift (correspond to ~106km)
568 would be denoted as LO_1, +2° longitude shift is LO_2, and so on. For clarity purpose, we
569 only illustrate altitude curves at z=50km (bottom line), z=54km (standard), and z=60km (upper
570 line) for subsequent statistical analysis.

571

572 We focus on the ECC (Figure 16 a: red points) at LO_0. Interestingly, the (red) scatter plot are
573 all positioned on the outermost edge part of the total combination scatter plots (grey). This
574 suggests that the aerosols at LO_0 (i.e. region closest to discontinuity front) are all at the
575 highest elevation amongst the aerosol distribution in the 10x10-region. This can be interpreted
576 as aerosols are being elevated towards higher altitudes by strong upwelling close to the
577 discontinuity front. Peralta et al. (2019) also observed these discontinuity features using IR1
578 images (sensitive to altitudes z~55-60km). This means that these observations show that the
579 observed discontinuity fronts were being elevated to higher altitudes. According to the analysis
580 using different altitude curves, the data shows that most of the TR4 at higher transmissions
581 align on the z=60km theoretical curve. In contrast, TR4 in lower transmissions are
582 progressively situated below the z=60km curve (about z=58km to z=54km). The interpretations
583 from altitudinal variations may suggest aerosols locating at lower altitudes for those in lower
584 transmissions. However, fractional mixing of smaller particles could also be a possibility.

585

586

[Figure 16]

587

588 Now, we will analyze the scatter plot progressing from LO_0 to LO_6 which would deliver a
 589 sense of altitude variability across regions away from the discontinuity front. To evaluate the
 590 transitions of scatter plot from one altitude curve to another, we incorporate RMSD (root-mean-
 591 square deviation) measurement for deviations of the observation points (from LO_0 to LO_6)
 592 to the respective theoretical altitude curves at: z=50km, 52km, 54km, 58km, 56km, and 60km
 593 (Table 10 and Figure 17). The RMSD is defined as:

$$\text{RMSD}(z) = \sqrt{\frac{1}{N} \sum_{i=1}^N [\text{TR}(i)_{1.735\mu\text{m}}^{\text{obs}} - \text{TR}_{1.735\mu\text{m}}^{\text{model}}(z, \text{TR}(i)_{2.26\mu\text{m}}^{\text{obs}})]^2} \quad (15)$$

594 where $\text{TR}_{1.735\mu\text{m}}^{\text{obs}}$ is observed 1.735 μm transmittance, $\text{TR}_{1.735\mu\text{m}}^{\text{model}}$ is computed by logarithmic-
 595 quartic polynomial approximation (not shown) for respective theoretical altitude (z) curve and
 596 observed 2.26 μm transmittance ($\text{TR}_{2.26\mu\text{m}}^{\text{obs}}$) where the difference between the observed and
 597 model can be obtained, and 'i' is for a pair of $\text{TR}_{2.26\mu\text{m}}^{\text{obs}}$ and $\text{TR}_{1.735\mu\text{m}}^{\text{obs}}$ number of order of
 598 observed transmittance $\text{TR}_{1.735\mu\text{m}}^{\text{obs}}$ and N is the total number of elements of observed
 599 transmittance $\text{TR}_{1.735\mu\text{m}}^{\text{obs}}$.

600

601 [Table 10a]

602 [Table 10b]

603 [Figure 17]

604

605 The distribution illustrates transitions from concentration in higher altitude z=58km at LO_0
 606 to settling at lower altitude z=52km at LO_3 (Figure 17). At LO_0, the highest probability of
 607 concentration is z=58km as the minimum of RMSD indicates. Then, more aerosol distribution
 608 is encompassing around z=52-54km from LO_3. Particles initially at z=58-60km altitudes also

609 descend into the lower altitudes as depicted where RMSD is highest for z=58-60km curve at
610 LO_3 (Figure 17).

611

612 Assuming the observation at LO_3 is due to temporal change as the discontinuity front
613 propagated away from this region (where spatial variability across ~300km is still
614 considerable), this can also be translated as where the particles have sink by ~5km (at LO_3)
615 at about 317km distance behind the region closest to the front (LO_0). Strong upwelling at the
616 ECC front (LO_0) ascending the mode 3 aerosol aloft as high up as z=58km altitudes. The
617 ECC propagates about ~20m/s faster than the background super-rotation speed (Peralta et al.,
618 submitted) leaving the uplifted particles behind to sink. (These interpretations are currently
619 based on assumptions where altitudes were the only factor being accounted for and yet to be
620 established). Estimating the particles to sink at LO_3 (~317km away from LO_0), the particles
621 took only ~0.2days to descent down to z=54km while the discontinuity front have already
622 traveled away by ~317km. For particles to descend by 5km in 0.2days as being observed, it
623 requires -0.3m/s sinking velocity.

624

625 However, particle's sedimentation speed is $\sim -0.3\text{m/s}$ from Stokes velocity of $\omega_{\text{sed}} = -\frac{2g\rho r^2}{9\eta} \sim$
626 -0.003m/s where $g \sim 8.7\text{ms}^{-2}$ is gravity acceleration, $\rho \sim 1.8 \times 10^3\text{kg m}^{-3}$, $r = 3.63\mu\text{m}$ for radius of
627 mode 3 particles, and $\eta \sim 1.5 \times 10^{-5}\text{kg m}^{-1}\text{s}^{-1}$ is the viscosity of CO₂ atmosphere (Imamura and
628 Hashimoto., 1998). Sedimentation at this speed would require ~19days to descend by 5km as
629 being observed. Thus, this could suggest that there could be an additional downwelling motion
630 that accelerates the sinking of the particles to be ~100 times faster than the Stokes velocity.
631 Look carefully at the boundary of the discontinuity, notice that there is a slight strip of bright
632 radiances (Figure 18). This may hint on strong downwelling force at regions around the
633 discontinuity front. This strong downwelling can propel the aerosols to sink at higher velocity

634 into the hot lower atmosphere where being evaporated causing higher number density by
635 vapors as illustrated in Figure19. In subsequent observations however, the bright strip is no
636 longer very visible. This may be due to the increasing convection further in the nightside where
637 downwelling is weakened.

638

639 [Figure 18]

640

641 From LO_3 to LO_6, the transmissions progressively getting lower to below ~0.25 in
642 TR(2.26 μ m) and ~0.45 in TR(1.735 μ m). This may indicate where accumulated large particles
643 sinking into denser part of the lower cloud deck while accumulating up to column density of
644 $N \sim (7 \text{ to } 8) \times 10^6$ particles cm^{-2} corresponding to optical thicknesses of $\tau \sim 8$ (i.e. TR~0.22)
645 (Figure 17). This would require ~6.90 mg cm^{-2} amount of vapor to condense into observed
646 optical thickness. While conserving volume, mode 3 conversion to mode 2' particles would
647 increase the optical thickness to $\tau \sim 29.2$. This correspond to lowering the TR down to TR~0.11
648 which is half the transmission level when only mode 3 was considered. Therefore, the
649 consideration for mixing of smaller particles should not be exempted. The RMSD
650 interpretation for proximity to altitudinal variations progressing from LO_0 to LO_6 may
651 suggest that the concentration of particles is located at $z \sim 52\text{km}$ at LO_6 (~600km away from
652 LO_0).

653

654 In overall, the aerosols in high transmissions can only be explained by elevating altitudes. On
655 the other hand, the lower transmissions underlying just below of mode 3 ($z=54\text{km}$) curve would
656 have two possibilities of considerations: 1. Decreasing altitudes, and/or 2. Mixture of smaller
657 size particles.

658

659
660
661
662
663
664
665
666
667
668
669
670
671
672
673
674
675

676
677
678
679
680

681

[Figure 19]

5.5. Investigation on the spatial variability of the ECC: August-27 data

For August-27 data, we focus on 08-27/20:03 data where its measurement is comparable to 08-18/15:33. Moving across 20:03/LO_0 to 20:03/LO_6 in Aug-27 (Figure 20a-c), the ECC-scatter (red) plot shows smooth transition from high altitudes ($z=56-58\text{km}$) to lower altitudes ($z=50\text{km}$). The RMSD for LO_0 to LO_6 also explicitly shows transition from high $z=54-60\text{km}$ to low $z=50\text{km}$ (Figure 21). This transitional trend from high altitude curve to low altitude curve can be related to 08-18/15:33 in Section 5.4.2. 20:03/LO_0 to 20:03/LO_6 corresponding to $\sim 633.6\text{km}$ in distance apart could be displaying two possible interpretations: 1. Spatial variation in LO_6 ($\sim 600\text{km}$ across from LO_0) owes to the BC at lower altitudes whereby the ECC would have already travelled away at higher altitudes; 2. When interpreted from temporal frame, this may be related to the rapid sinking velocity by strong downwelling. The similarity between 08-27/20:03 to 08-18/15:33 longitudinal variation (LO_0 to LO_6) shows that the concentration of aerosols begin from locating at higher altitude curves $z\sim 56-58\text{km}$, then transiting to the lower altitude curves at $z=50\text{km}$ and $z=52\text{km}$ for 08-27/20:03 and 08-18/15:33 respectively (according to interpretation RMSD plots in Figure 17 and Figure 21).

[Figure 20]

[Figure 21]

[Table 11a]

[Table 11b]

6. Conclusion

682 The ‘Restoration by Deconvolution’ (RD) method has improved the photometric accuracy by
683 true contrast which has enabled photometric studies on the ‘Enormous Cloud Cover’ (ECC).
684 The ECC events on Aug-18 and Aug-27 2016 are the largest discontinuity features observed
685 by Akatsuki/IR2 with good spatial and temporal tracking. Thorough statistical photometric
686 analyses in RD processed data have been performed on both the Enormous Cloud Cover (ECC)
687 and Background Clouds (BC) to characterize the spatial variabilities of each cloud layer.
688 Utilizing radiative transfer, the spatial variations observed from the ECC have been examined
689 for the distribution of particle modes (mode 1, mode 2, mode 2’, and mode 3) where mode 1
690 have been ruled out from our analysis. Other than considering for distribution of smaller
691 particles, possible altitude variations were considered for the observed ECC’s spatial variations.
692 The locations of aerosol distribution in the ECC were found to vary starting from higher
693 altitudes $z=56-58\text{km}$ (at LO_0) down to $z=50-52\text{km}$ (at LO_6 i.e. $\sim 600\text{km}$ away). Also, it has
694 been found that the ECC’s discontinuity front experiences both strong upwelling and
695 downwelling motions that sink the large particles at $\sim -0.3\text{m/s}$ that is faster than the
696 sedimentation rate from Stokes velocity $\sim -0.003\text{m/s}$. Such statistical analysis for altitudinal
697 variations of the ECC has never been explored before and hence this could be an opening to
698 more investigations of the peculiar yet intriguing Enormous Cloud in Venusian atmosphere.
699 The mechanism of production and maintenance of the cloud dynamics such as the ECC that
700 absorbs energy from both above and below of the clouds may possibly be related to the
701 maintenance of the super-rotation induced by thermal tides in the cloud top layers. Last but not
702 least, the availability of our processed data will open new doors to exploring identities of other
703 interesting morphologies in hope to explore the cloud dynamics in the lower clouds that could
704 hint on the mechanisms of the unsolved Venus’s super-rotation questions.

705

706 **Appendix**

707 **Appendix A. Finding dayside F Factor to calibrate RT-calculated dayside**

708 From the development of RD-method, ‘convolved models by PSF (CVM)’ have already been
 709 prepared to simulate observation expectations at dayside F=1.0. Then, we can calibrate for the
 710 actual dayside F factor by comparing the light spreading in CVM (at F=1.0) to L2B
 711 observations. The calibration was performed by selecting a 25-pixels² size ‘box’ region at
 712 constant pixel-distance away from the Venus’s dayside limb for both CVM and L2B images
 713 where radiance values in the selected ‘box’ were averaged for CVM and L2B respectively.
 714 The F factor for 2.26μm is hence:

715
$$F(2.26\mu\text{m}) = \sum \frac{\overline{\text{CVM}}}{\overline{\text{L2B}}}$$

716
 717 where $\overline{\text{CVM}}$ and $\overline{\text{L2B}}$ are averaged radiances from the 25-pixels² box at constant pixel-
 718 distances away from the Venus’s dayside limb.

719
 720 Then, the F factor for 1.735μm can be computed as:

721
$$C = \sum \frac{\overline{\text{MDD}}_{1.735\mu\text{m}}}{\overline{\text{MDD}}_{2.26\mu\text{m}}}$$

722
$$R = \frac{k_{2.26\mu\text{m}}}{C}$$

723
$$F(1.735\mu\text{m}) = R \times F(2.26\mu\text{m})$$

724 where $\overline{\text{MDD}}_{2.26\mu\text{m}}$ and $\overline{\text{MDD}}_{1.735\mu\text{m}}$ are mean radiances of total integrated flux from the
 725 Model Daysides (MDD) for 2.26μm and 1.735μm filter respectively, and $k_{2.26\mu\text{m}}$ is $k_{2.26\mu\text{m}} =$
 726 $(8.4277 \times 10^{-4})\alpha^2 - (2.2731 \times 10^{-1}) + 17.979$ from Satoh et al., (submitted) which is a
 727 calibration factor to adjust 2.26μm dayside intensities into 1.735μm filter.

728
 729 Finally, the corrected Model Daysides (MDD’) can be expressed as the following

730
$$MDD'_{2.26\mu\text{m}} = MDD_{2.26\mu\text{m}} \times F(2.26\mu\text{m})$$

731
$$MDD'_{1.735\mu\text{m}} = MDD_{1.735\mu\text{m}} \times F(1.735\mu\text{m})$$

732 Table A summarizes the Dayside F factors obtained from the above calculations.

733 [Table A]

734

735 **Appendix B. Photometric restoration by RD and RS methods**

736 Synthetic models simulating Venus observations under influence by camera's conditions (PSF,
737 dayside contamination, and saturation) are generated to test restorative strengths of the two
738 methods: RD and RS. For this test, we use 2016/08/18 15h RD-restored resultant as nightside
739 answer image (RRD), radiative transfer calculated dayside (RTD), and known model-PSF. Then,
740 we can synthesize the full Venus disk (MDV) being convolved by model-PSF to simulate the
741 typical observation condition by IR2 camera. RD and RS processes are performed on the
742 convolved image where the results can be compared with the known answer image using scatter
743 plots of resultants to answer image (Figure A1).

744

745 To clarify here, there are two Restoration-by-Subtraction (RS) methods: Restoration-by-
746 Subtraction 'Subtraction-only' (RSS) (Sato et al., submitted), and Restoration-by-Subtraction
747 'using PSF' (RSP). Both RSS and RSP incorporates the same concept where both methods
748 minimize contamination by dayside PSF. Thus, RSP performed here intends to simulate RSS
749 in the synthetic case. RSS performs subtraction by differentiating two filters (Section 3.3). On
750 the other hand, RSP simulates the dayside light spread by convolving the radiative transfer
751 calculated dayside ('Convolved Radiative Transfer Dayside' = 'CRTD') by model-PSF. Then,
752 the image is restored by subtraction (RSP): $CLN = L2B - CRTD$.

753

754 RSP-answer scatter plot giving ~ 0.7 (< 1) slope indicates inability of RS method to recover
755 light scattered away from each pixel due to PSF. For bright pixels, RS method does not recover
756 light spread by PSF into adjacent pixels. In dark pixels, RS method cannot remove remaining
757 radiances of light spread by adjacent brighter pixels after subtraction being ceased when overall
758 minimum contamination is achieved. This results in the y-intercept offset value of ~ 0.005
759 where ideal restoration should bring the y-intercept closer to 0.

760

761 In contrast, RD-answer scatter plot's slope of 0.98 (~ 1) shows the working of deconvolution
762 to recover light spread into adjacent pixels back to its original source. Imagine a bright pixel
763 in the nightside, RD works by re-collecting light spread by PSF into adjacent pixels back to its
764 original position. As for a dark pixel in the nightside, the influence of light spread by adjacent
765 brighter pixels can be removed during deconvolution process. This gives the almost ~ 0 y-
766 intercept in the RD-answer scatter plot.

767

768 Figure A2 illustrates the comparison of both RD and RS method. The RD-RS scatter plot
769 illustrates higher slope ~ 1.3 (> 1) indicating RD has more photometry restored for bright pixels
770 when compared to RSS. The negative y-intercept also shows that darker pixels in nightside are
771 better recovered from influences of adjacent pixels in RD to that of RS.

772 [Figure A1]

773 [Figure A2]

774

775 **Declarations**

776 **Ethics approval and consent to participate**

777 Not applicable

778

779 **Consent for publication**

780 Not applicable

781

782 **List of abbreviations**

783 PV: Pioneer Venus

784 LCPS: Cloud Particle Size Spectrometer

785 NIMS: Near Infrared Mapping Spectrometer

786 VIRTIS: Visible and Infrared Thermal Imaging Spectrometer

787 VEx: Venus Express

788 PSF: point spread function

789 RMSD: Root-mean-square deviation

790 ROI: Region of Interest

791 RSS: Restoration by Simple Subtraction

792 RD: Restoration by Deconvolution

793 MDD: Model Dayside Disk

794 CLN: Cleaned Night

795 Model Dayside + Nightside: MDN

796 CVM: Convolved Model

797 COM: Combined frame

798 RDD: RD-processed Data

799 ECC: Enormous Cloud Cover

800 BC: Background Cloud

801 SD: Standard Deviation

802 R-L: Richardson-Lucy

803

804 **Availability of data and materials**

805 The authors are going to archive and publish the RD processed data to make available for
806 public use.

807

808 **Competing Interests**

809 None

810

811 **Funding**

812 CWV was supported by the Japanese Government Monbukagakusho (MEXT) scholarship to
813 conduct this study.

814

815 **Authors' contributions**

816 CWV is responsible for all elements of this manuscript. TS calibrated the temperature
817 dependent behavior of IR2 data and has supervised CWV in conduct of this study within
818 doctoral course. TMS provided radiative transfer calculations for dayside reflectance. TH
819 corrected the image navigation of the spacecraft using limb fitting technique.

820

821 **Acknowledgements**

822 The authors are grateful to all members of Akatsuki (Planet-C) to have accomplished
823 successful observations of Venus. Special thanks to Dr. J. Peralta who has been reliable to
824 discuss about the intriguing findings in this paper. Furthermore, the authors would like to
825 express gratitude to Dr. K. McGouldrick, Dr. E. Young, and Dr. S. Limaye who have been
826 contributive to Akatsuki mission and scientific discussions. Not to mention, Dr. T. Oba has
827 also been supportive in sharing his knowledge on deconvolution technique performed on
828 *Hinode* observations. Finally, the authors are also indebted to Prof. M. Kimata, Ritsumeikan

829 University and manufacturers of IR2 (Sumitomo Heavy Industries, Ltd., Mitsubishi Electronic
830 Company MELCO, Nikon, Magoshi, and Fujitoku and Barr Associates) for the development
831 of the Akatsuki/IR2 camera.

832

833 **Authors' information**

834 TS is the Principle Investigator of Akatsuki/IR2.

835

836 **Endnotes**

837 None

838

839 **References**

840 Belton MJS et al (1991) Images from Galileo of the Venus Cloud Deck. *Science* 253:1531-
841 1536. <https://doi.org/10.1126/science.253.5027.1531>

842

843 Baker RD, Schubert G, Jones PW (1998) Cloud-level penetrative compressible convection in
844 the Venus atmosphere. *Journal of Atmospheric Sciences* 55, 3-18.

845

846 Carlson R et al (1991) Galileo infrared imaging spectrometer measurements at Venus. *Science*
847 253, 1541-1548.

848

849 Carlson R et al (1993) Variations in Venus cloud particle properties: a new view of Venus's
850 cloud morphology as observed by Galileo near-infrared mapping spectrometer. *Planetary and*
851 *Space Science* 41: 477-485.

852

853 Esposito LW, Knollenberg RG, Marov MY, Toon OB, and Turco RP (1983) The clouds and
854 hazes of Venus. In *Venus*, edited by Hunten, DM et al, The University of Arizona Press, Tucson,
855 pp. 484-564.

856

857 Grinspoon DH et al (1993) Probing Venus's cloud structure with Galileo NIMS, *Planetary and*
858 *Space Science* 41(7), 515-542.

859

860 Haus R, Kappel D, Arnold G (2015) Lower atmosphere minor gas abundances as retrieved
861 from Venus Express VIRTIS-M-IR DATA AT 2.3 μ m. *Planetary and Space Science* 105, 159-
862 174.

863

864 Hueso R, Peralta J, Sanchez-Lavega A (2012) Accessing the long-term variability of Venus
865 winds at cloud level from VIRTIS-Venus Express. *Icarus* 217, 585-598.

866

867 Horinouchi T (2017) Equatorial jet in the lower to middle cloud layer of Venus revealed by
868 Akatsuki. *Nature Geoscience*. 10, 646-651.

869

870 Imamura T, Hashimoto GL (1998) Venus cloud formation in the meridional circulation.
871 *Journal of Geophysical Research* 103, 31349-31366.

872

873 Imamura T, Higuchi T, Maejima Y., Takagi M, Sugimoto N, Ikeda K, Ando H (2014) Inverse
874 insolation dependence of Venus's cloud-level convection. *Icarus* 228, 181-118.

875

876 Knollenberg RG and Hunten DM (1980) The microphysics of the clouds of Venus: Results of
877 the Pioneer Venus Particle Size Spectrometer experiment. *Journal of Geophysical Research.*,
878 85(A13), 8039-8058.

879

880 McGouldrick K, Momary TW, Baines KH, and Grinspoon DH (2012) Quantification of middle
881 and lower cloud variability and mesoscale dynamics from Venus Express/VIRTIS observations
882 at 1.74 μ m. *Icarus* 217, 615-628.

883

884 McGouldrick K (2017) Effects of variation in coagulation and photochemistry parameters on
885 the particle size distributions in the Venus clouds. *Earth Planets Space* 69:161.
886 <https://doi.org/10.1186/s40623-017-0744-x>

887

888 Murakami S, Satoh T, McGouldrick K, Yamamoto Y, Hashimoto GL (2018) Venus Climate
889 Orbiter Akatsuki IR2 calibrated data v1.0, VCO-V-UVI-3-CDR-V1.0. In: NASA Planetary
890 Data System. <https://doi.org/10.17597/ISAS.DARTS/VCO-00003>.

891

892 Palmer KF and Williams D (1975) Optical Constants of Sulfuric Acid; Applications to the
893 Clouds of Venus?. *Applied Optics* Vol. 14, No.1.

894

895 Peralta J et al (2018) Nightside Winds at the Lower Clouds of Venus with Akatsuki/IR2:
896 Longitudinal, Local Time, and Decadal Variations from Comparison with Previous
897 Measurements. *Astrophysical Journal Supplement Series*. 239:29 (17pp).
898 <https://doi.org/10.3847/1538-4365/aae844>

899

900 Peralta J et al (2019a) Morphologies and Dynamics of Venus's Middle Clouds with
901 Akatsuki/IR1. *Geophysical Research Letters*. 46(5), 2399-2407.
902

903 Peralta J et al (submitted) A long-lived disruption on the lower clouds of Venus. Submitted to
904 *Geophysical Research Letters*.
905

906 Pollack JB et al (1979) Nature of the ultraviolet absorber in the Venus clouds – Inferences
907 based on Pioneer Venus data. *Science* 205(4401):76-79.
908 <https://doi.org/10.1126/science.205.4401.76>
909

910 Ragent B et al (1985) Particulate matter in the Venus atmosphere. *Adv. Space Res. Vol 5,*
911 *No.11, p85-115.*
912

913 Satoh T et al (2016) Development and in-flight calibration of IR2: 2- μ m camera onboard
914 Japan's Venus orbiter, Akatsuki. *Earth Planets Space* 68:74. [https://doi.org/10.1186/s40623-](https://doi.org/10.1186/s40623-016-0451-z)
915 [016-0451-z](https://doi.org/10.1186/s40623-016-0451-z)
916

917 Satoh T et al (2017) Performance of Akatsuki/IR2 in Venus orbit: the first year. *Earth Planets*
918 *Space* 69:154. <https://doi.org/10.1186/s40623-017-0736-x>
919

920 Satoh T et al (submitted). Venus nightside photometry with “cleaned” Akatsuki/IR2 data:
921 Aerosol properties and variations of carbon monoxide. Submitted to *Icarus*.
922

923 Sato TM et al (2020) Dayside cloud top structure of Venus retrieved from Akatsuki IR2
924 observations. *Icarus* 345, 113-682.

925

926 Seiff, A (1982) Dynamical implications of the observed thermal contrast in Venus's upper
927 atmosphere. *Icarus* 51, 574-592.

928

929 Stamnes K, Tsay SC, Wiscombe WJ, Jayaweera K (1988) Numerically stable algorithm for
930 discrete-ordinate-method radiative transfer in multiple scattering and emitting layered media.
931 *Applied Optics* 27, 2502-2509.

932

933 Titov DV, Ignatiev NI, McGouldrick K, Wilquet V, Wilson CF (2018) Clouds and Hazes of
934 Venus. *Space Science Reviews*, 214:126

935

936 **Figure Legends**

937 **Figure 1** -Level 2b (L2B) data example showing influence of dayside light spread due to IR2
938 camera's point spread function (PSF) and saturation. Saturated pixels were given -100 W m^{-2}
939 $\text{sr}^{-1} \mu\text{m}^{-1}$ units offset: (Top-left) 08-18/15:33 $2.26\mu\text{m}$, (Top-right) 08-27/20:03 $2.26\mu\text{m}$,
940 (Bottom-left) 08-18/15:32 $1.735\mu\text{m}$, (Bottom-right) 08-27/20:02 $1.735\mu\text{m}$

941

942 **Figure 2** – (a) Image resultants from Step 2 to Step 5 of RD method i.e. (Step 2) MDD & CLN,
943 (Step 3) CVM, (Step 4) COM, and (Step 5) RDD; (b) Image preparations from Step 2 to Step
944 5 of RD method i.e. (Step 2) MDD (x 0.01 to scale to other images) & CLN, (Step 3) CVM,
945 (Step 4) COM, and (Step 5) RDD.

946

947 **Figure 3** – Loss to Off-Disk/Total Flux plot against spacecraft distance from Venus in
948 Logarithmic scale for $2.02\mu\text{m}$ dayside observation data (L2B) below 45° phase angle (orbit
949 14,15, and 16), and synthetic dayside convolved by model-PSF: Red (orbit 14), Yellow (orbit
950 15), Orange (orbit 16).

951

952 **Figure 4** – (Left) Example L2B data (2016-08-18 21:33) in $2.26\mu\text{m}$ showing image was
953 trimmed by [129:896, 385:1024] 'Region of Interest' (ROI). The image is in the original
954 orientation of the downlink data where North is downwards. (Right) Preparation of $2048 \times$
955 2048 pixels^2 size frame to accommodate simulation of light spread by PSF outside ROI frame
956 and saturated pixels being replaced. In this example, the larger canvas outside ROI frame
957 enables loss photometry up to $\sim 14\%$ to be recovered where light spreading can be pulled back
958 by deconvolution. The yellow arrows point on the PSF tail extension spreading light outside
959 the ROI frame.

960

961 **Figure 5** – RDD image example in $2.26\mu\text{m}$ where the measurements for radiance contrast will
962 be illustrated in Figure 8: (a) $2.26\mu\text{m}$; (b) $1.735\mu\text{m}$

963

964 **Figure 6** – 10° longitude x 10° latitude pixel² size ‘box’ to obtain average radiance within the
965 selected region both in the optically thick enormous cloud and bright background (10°
966 longitude apart) to measure the averaged transmittance of radiation through the enormous cloud
967 feature. The boxes are shifted longitudinally by estimated speed in between the 2-hr
968 observations. Image examples shown here are 2-hr intervals of limb darkening corrected RD-
969 restored data where the wind speed of the enormous cloud is estimated at 90 m/s. (a) 08-
970 18/15:33 to 21:33; (b) 08-27/20:03 to 22:03

971

972 **Figure 7** - Average radiances of ‘box region’ in ECC and BC as selected in Figure 6a obtained
973 for RDD images. Fogging factor x 10 range is included: (a) Aug-18 in $2.26\mu\text{m}$; (b) Aug-18 in
974 $1.735\mu\text{m}$

975

976 **Figure 8** - Average radiances of ‘box region’ in ECC and BC as selected in Figure 6b obtained
977 for RDD images. Fogging factor x 10 range is included: (a) Aug-27 in $2.26\mu\text{m}$; (b) Aug-27 in
978 $1.735\mu\text{m}$

979

980 **Figure 9** - Radiative transfer calculation for transmittance by additional optical thickness of
981 single-mode aerosols (mode 1, mode 2, mode 2’, and mode 3) between 54 to 56 km altitude in:
982 (a) $2.26\mu\text{m}$; (b) $1.735\mu\text{m}$.

983

984 **Figure 10** – Observed Transmittance (TR) with associated uncertainty range plotting over
985 theoretical Transmittance (TR) computed by radiative transfer for different particle size modes
986 (mode 1, mode 2, mode 2', mode 3).

987

988 **Figure 11** – Standard deviation of CRD to L2B images in bins of 10° incident angles for: (a)
989 $2.26\mu\text{m}$; (b) $1.735\mu\text{m}$. There are no data for incident angles before 120° due to saturation.

990

991 **Figure 12**– Total combinations of 4x4-regions' transmission ratios plotted over particle mode
992 theoretical curves (mode 1, mode 2, mode 2' mode 3) showing alignment around mode 3 and
993 slightly reaching mode 2' theoretical curves.

994

995 **Figure 13** – (a) Case-L in which to lower the transmissions. This is divided into two sub-groups.
996 'Case-L(BC)' where I_{BC} is brighter than 'normal' intensity and 'Case L(ECC)' where I_{ECC} is
997 darker than normal intensity; (b) Case-H in which to increase to higher transmissions. This is
998 divided into two sub-groups. 'Case-H(BC)' where I_{BC} is darker than 'normal' intensity and
999 'Case L(ECC)' where I_{ECC} is brighter than normal intensity

1000

1001 **Figure 14** – Theoretical transmittance calculated for mode 3' ranging from $\bar{r}=2.0\mu\text{m}$ to $4.5\mu\text{m}$
1002 in $0.25\mu\text{m}$ intervals, and one fifth width of size distribution of mode 3 to the original denoted
1003 as '3.65 μm _sig', and mode 3 is $3.65\mu\text{m}$ mean radius. (Red Dots) are from previous Figure 13a
1004 and 13b representing I_{ECC} points.

1005

1006 **Figure 15** - Radiative transfer calculations for emissions by single-mode aerosols (only mode
1007 3 for this study) at different altitudes varying from 48-60km (at 2km intervals).

1008

1009 **Figure 16** – Combination scatter plots within 10x10region with resolution of 4x4-region
1010 statistical analysis. (Red) Transmission distribution of the Enormous Cloud Cover ‘ECC’.
1011 (Blue) Transmission distribution of the Background Cloud ‘BC’ in 08-18/15:33: (a) LO_0,
1012 (b) LO_3, (c) LO_6

1013

1014 **Figure 17** – RMSD for longitudinal distance away from discontinuity front (spatial variation):
1015 08-18/15:33. Left y-axis is RMSD and Right y-axis optical depths.

1016

1017 **Figure 18**– Close up image of RD-data (blue curve line) discontinuity front, (yellow arrow)
1018 bright downwelling features. (a) for 08-18/15:33, 17:33, 19:33, and 21:33. Note on the bright
1019 strip just after the front is most prominent at 15:33, then decreasing gradually in radiance to
1020 21:33; (b) 08-27/20:03 and 22:03.

1021

1022 **Figure 19** – Schematics of ECC

1023

1024 **Figure 20** – Combination scatter plots within 10x10region with resolution of 4x4-region
1025 statistical analysis. (Red) TR4 of the Enormous Cloud Cover ‘ECC’. (Blue) Transmission
1026 distribution of the Background Cloud ‘BC’ in 08-27/20:03: (a) LO_0, (b) LO_3, (c) LO_6

1027

1028 **Figure 21** – RMSD for longitudinal distance away from discontinuity front (spatial
1029 variation): 08-27/20:03. Left y-axis is RMSD and Right y-axis optical depths.

1030

1031 **Figure A1**- Comparison of restorative strengths in RD and RSS method. (Green) RD-answer
1032 scatter plot and (Red) RSS-answer scatter plot.

1033 **Figure A2** - RD-RSS scatter plot showing that RD restoration could restore more loss
1034 photometry than RSS method

1035

1036 **Tables**

1037 **Table 1** – Summary of Venus observations in 2.26 μm and 1.735 μm filters used in this study.

1038 a. 2.26 μm L2B data

1039 b. 1.735 μm L2B data

1040

1041 **Table 2** – Summary of denotations used for RD-method in this paper

1042

1043 **Table 3** – Aerosol properties set in radiative transfer computation

1044 b. Wavelength dependent cross section extinction cross sections (k_{ext}) and single scattering

1045 albedos (ω) for particles in 2.26 μm and 1.735 μm

1046

1047 **Table 4** – Calibration for Fogging values

1048 a. 2.26 μm filter

1049 b. 1.735 μm filter

1050

1051 **Table 5** - Transmittance of the Enormous cloud measured within ‘photometrically-stable

1052 region (incident angle $> 130^\circ$)’ for Aug-18 IECC and IBC are averaged intensity of the box

1053 region in $\text{Wm}^{-2}\text{sr}^{-1}\mu\text{m}^{-1}$ unit, whilst TR is transmittance.

1054

1055 **Table 6** - Coefficients for computing τ from Transmittance

1056

1057 **Table 7** – Optical thickness of the Enormous cloud measured within ‘photometrically-stable
1058 region (incident angle>130°)’

1059

1060 **Table 8** – Calculations for H₂SO₄ particles’ properties observed in the ECC measured within
1061 ‘photometrically-stable region (incident angle>130°)’ for 10x10-region.

1062 a. Column Density

1063 b. Column Mass

1064

1065 **Table 9** – Statistical analysis for I_{ECC} and I_{BC} combinations in 4x4-regions

1066 a. Tabulation of all possible combinations of the $\left(TR = \frac{I_{ECC}}{I_{BC}} \right)$ measurements for Case L
1067 and Case H. $f = 0.8$ is chosen to include about half the data points and sigma is the standard
1068 deviation of TR4.

1069 b. Extreme cases of I_{BC} and I_{ECC} to lower TR4 (Case-L) or to increase transmissions to
1070 higher TR4 (Case-H)

1071

1072 **Table 10** – RMSD from altitude curves and optical thickness range for longitudinal variation
1073 from LO_0 to LO_6 measurements for 08-18/33

1074 a. RMSD of $TR_{1.735\mu m}^{obs}$ to $TR_{1.735\mu m}^{model}$ from different altitude curves from LO_0 to LO_6

1075 b. Optical Depths range where ‘Min’ is minimum, ‘Max’ is maximum values of τ

1076

1077 **Table 11** – RMSD from altitude curves and optical thickness range for longitudinal variation
1078 from LO_0 to LO_6 measurements for 08-27/20:02

1079 a. RMSD of $TR_{1.735\mu m}^{obs}$ to $TR_{1.735\mu m}^{model}$ from different altitude curves from LO_0 to LO_6

1080 b. Optical Depths range where ‘Min’ is minimum, ‘Max’ is maximum values of τ

1081

1082 **Table A** – Dayside Calibration Factors

1083 a. 2.26 μm

1084 b. 1.735 μm

Figures

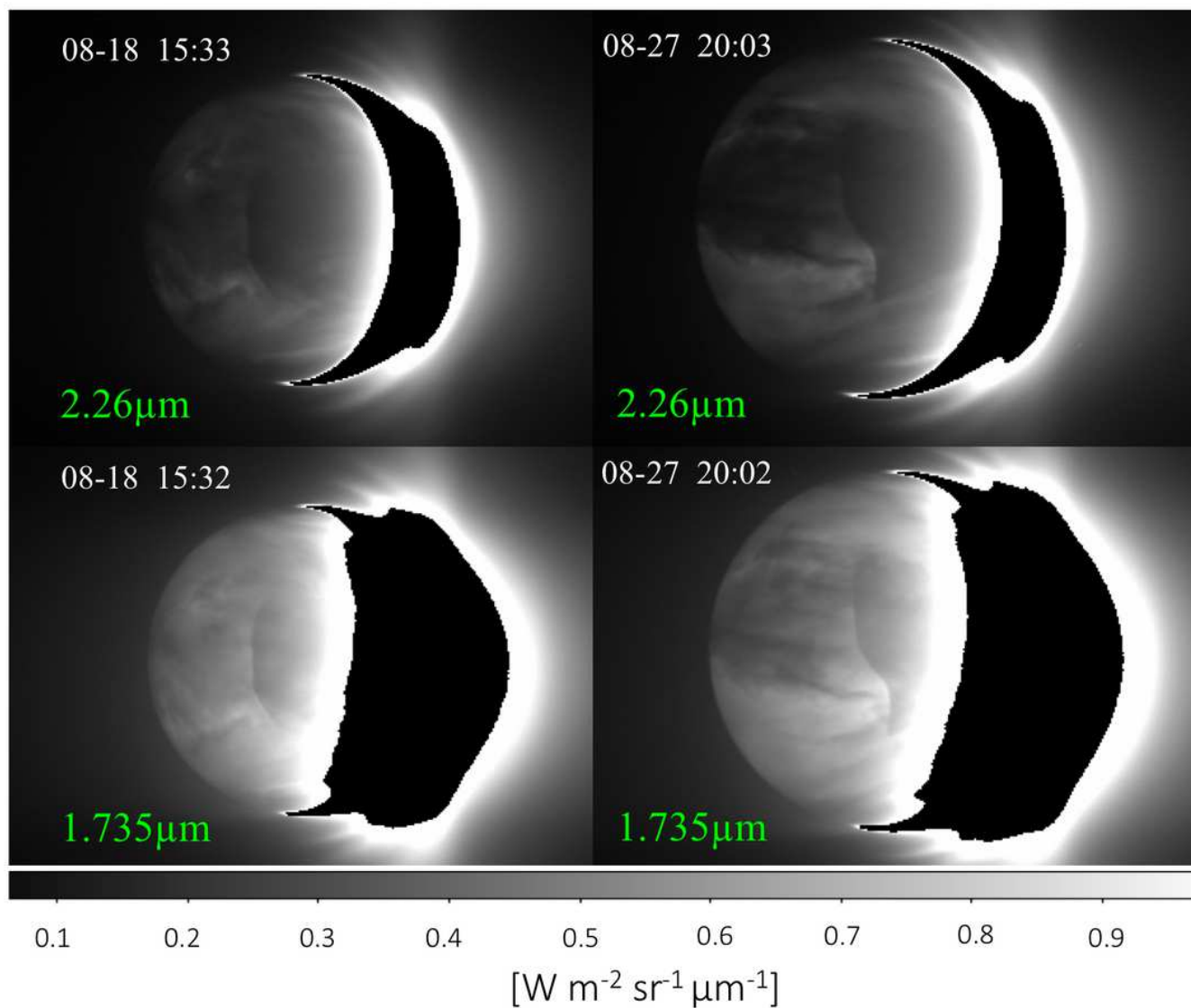
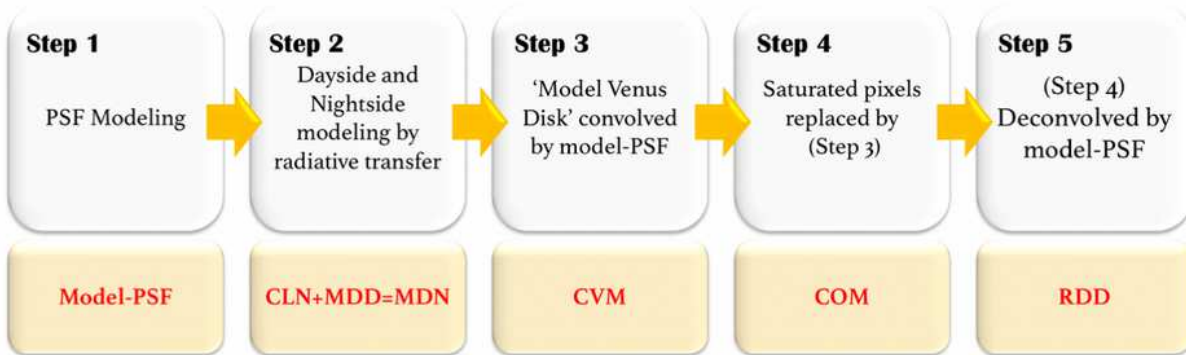


Figure 1

Level 2b (L2B) data example showing influence of dayside light spread due to IR2 camera's point spread function (PSF) and saturation. Saturated pixels were given -100 $W m^{-2} sr^{-1} \mu m^{-1}$ units offset: (Top-left) 08-18/15:33 2.26 μm , (Top-right) 08-27/20:03 2.26 μm , (Bottom-left) 08-18/15:32 1.735 μm , (Bottom-right) 08-27/20:02 1.735 μm

(a) Flowchart of RD-method from Step 1 to Step 5



(b) Sequential Image Preparations from Step 1 to Step 5

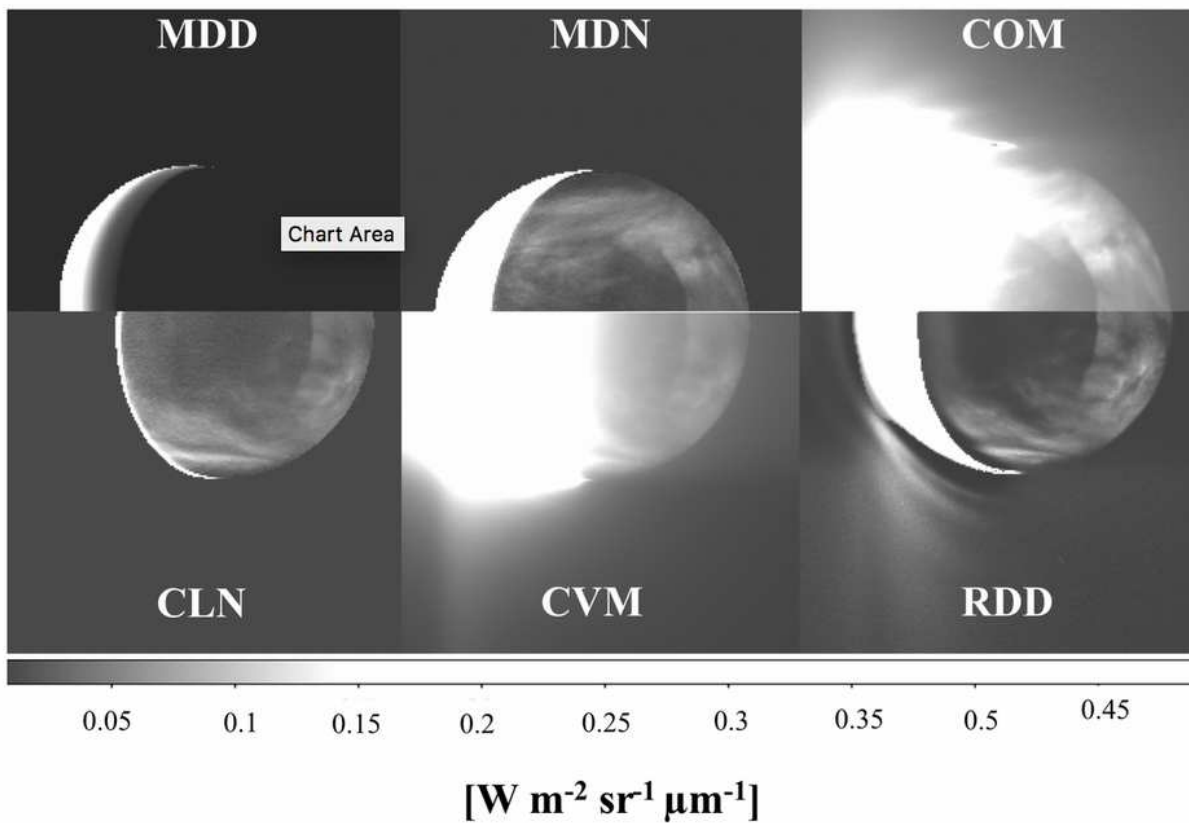


Figure 2

(a) Image resultants from Step 2 to Step 5 of RD method i.e. (Step 2) MDD & CLN, (Step 3) CVM, (Step 4) COM, and (Step 5) RDD; (b) Image preparations from Step 2 to Step 5 of RD method i.e. (Step 2) MDD (x 0.01 to scale to other images) & CLN, (Step 3) CVM, (Step 4) COM, and (Step 5) RDD.

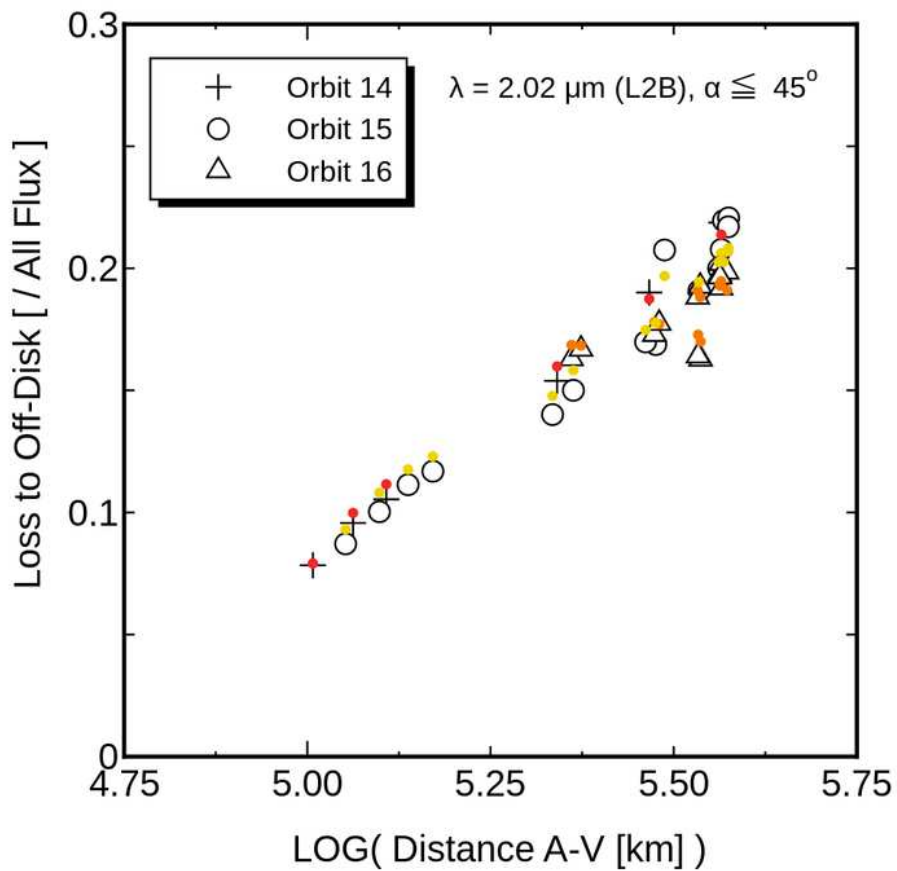


Figure 3

Loss to Off-Disk/Total Flux plot against spacecraft distance from Venus in Logarithmic scale for $2.02\mu\text{m}$ dayside observation data (L2B) below 45° phase angle (orbit 14,15, and 16), and synthetic dayside convolved by model-PSF: Red (orbit 14), Yellow (orbit 15), Orange (orbit 16).

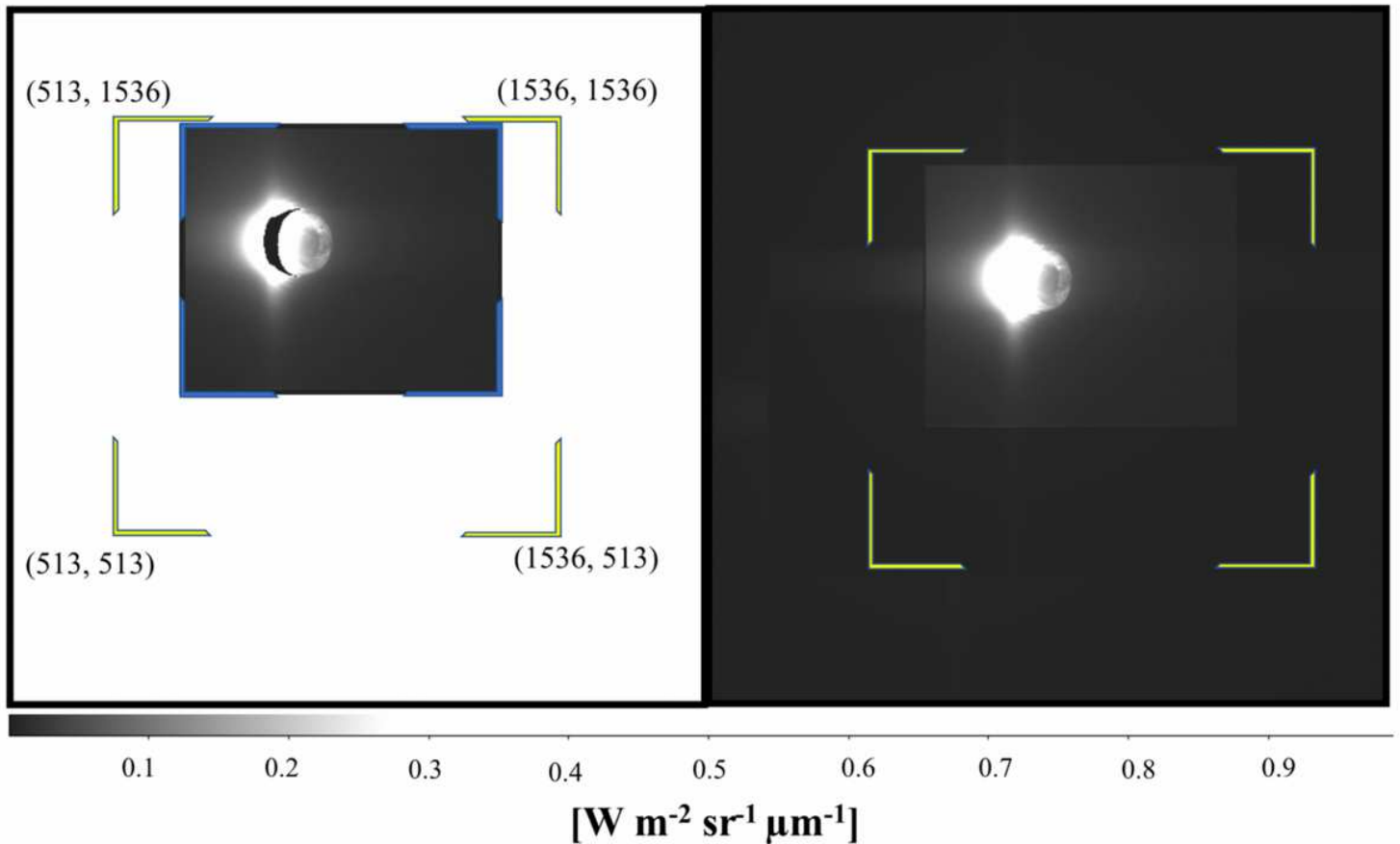
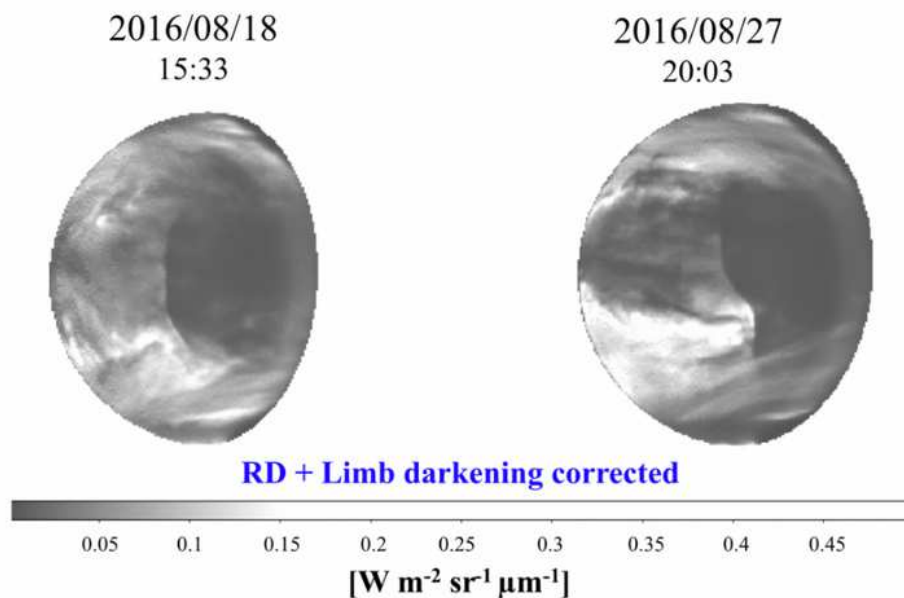


Figure 4

(Left) Example L2B data (2016-08-18 21:33) in $2.26\mu\text{m}$ showing image was trimmed by [129:896, 385:1024] 'Region of Interest' (ROI). The image is in the original orientation of the downlink data where North is downwards. (Right) Preparation of 2048×2048 pixels² size frame to accommodate simulation of light spread by PSF outside ROI frame and saturated pixels being replaced. In this example, the larger canvas outside ROI frame enables loss photometry up to $\sim 14\%$ to be recovered where light spreading can be pulled back by deconvolution. The yellow arrows point on the PSF tail extension spreading light outside the ROI frame.

(a) RDD: 2.26 μm



(b) RDD: 1.735 μm

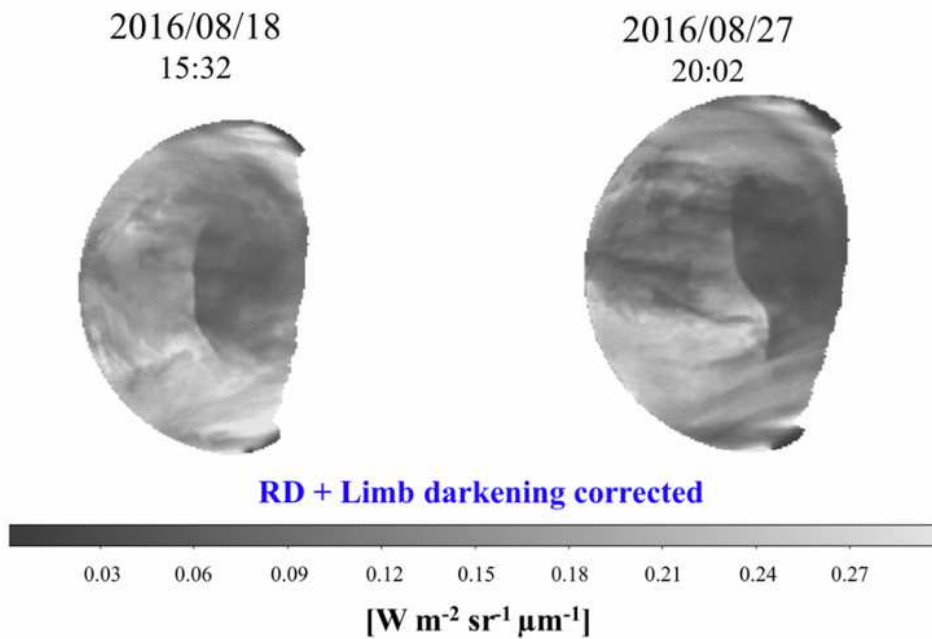
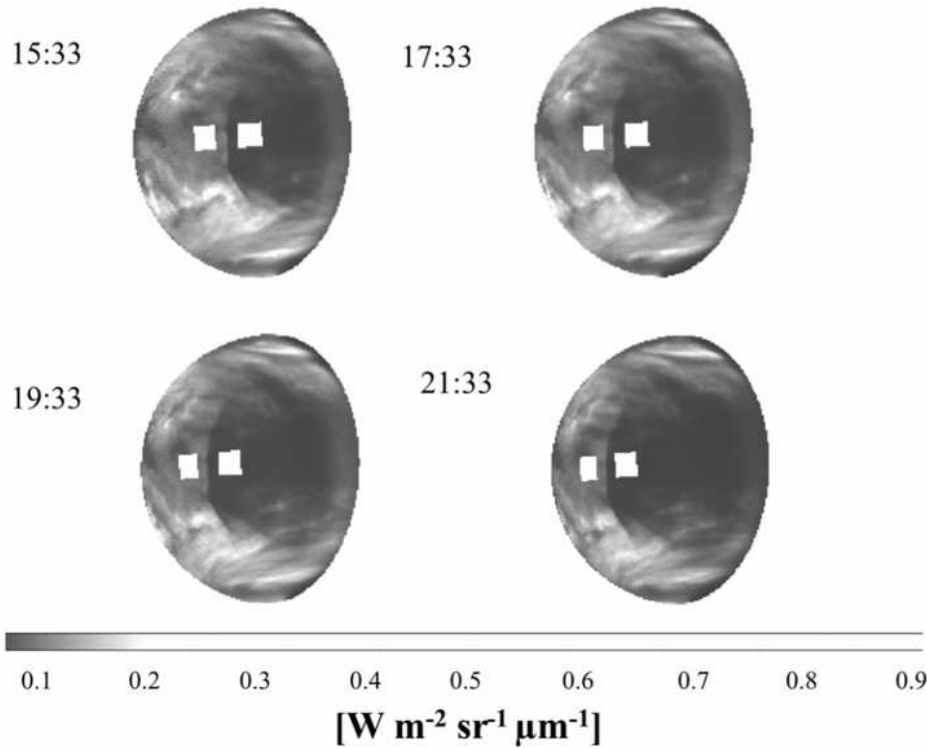


Figure 5

RDD image example in 2.26 μm where the measurements for radiance contrast will be illustrated in Figure 8: (a) 2.26 μm ; (b) 1.735 μm

(a) 2016-08-18



(b) 2016-08-27

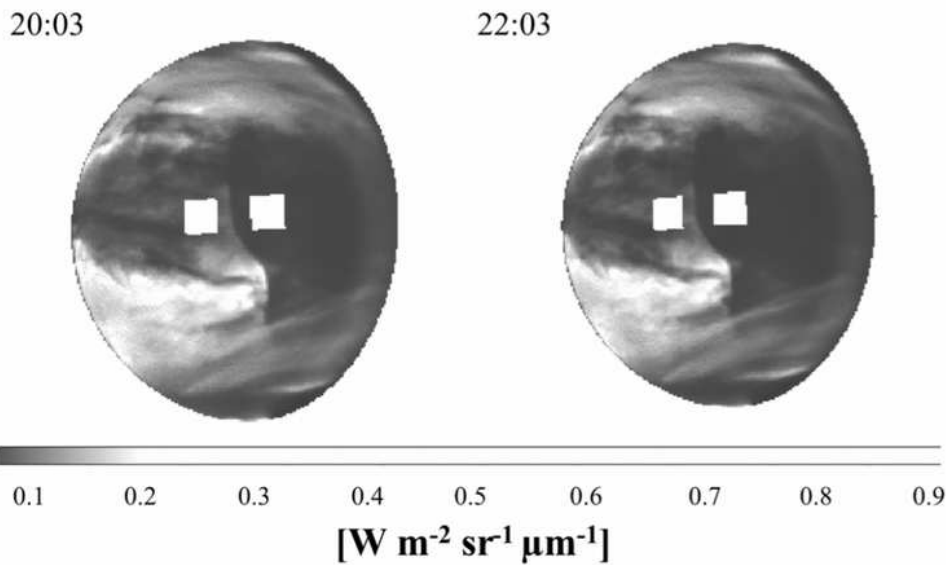
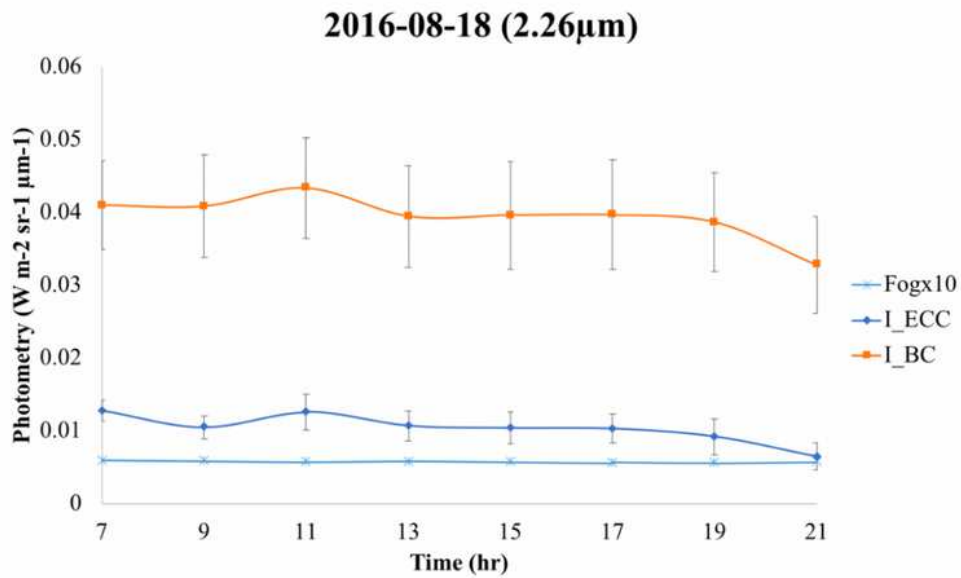


Figure 6

10° longitude x 10° latitude pixel² size 'box' to obtain average radiance within the selected region both in the optically thick enormous cloud and bright background (10° longitude apart) to measure the averaged transmittance of radiation through the enormous cloud feature. The boxes are shifted longitudinally by estimated speed in between the 2-hr observations. Image examples shown here are 2-hr intervals of limb

darkening corrected RD-restored data where the wind speed of the enormous cloud is estimated at 90 m/s. (a) 08-18/15:33 to 21:33; (b) 08-27/20:03 to 22:03

(a) I_{ECC} and I_{BC} measurements from 10x10-region for 2016-08-18 RDD: $2.26\mu\text{m}$



(b) I_{ECC} and I_{BC} measurements from 10x10-region for 2016-08-18 RDD: $2.26\mu\text{m}$

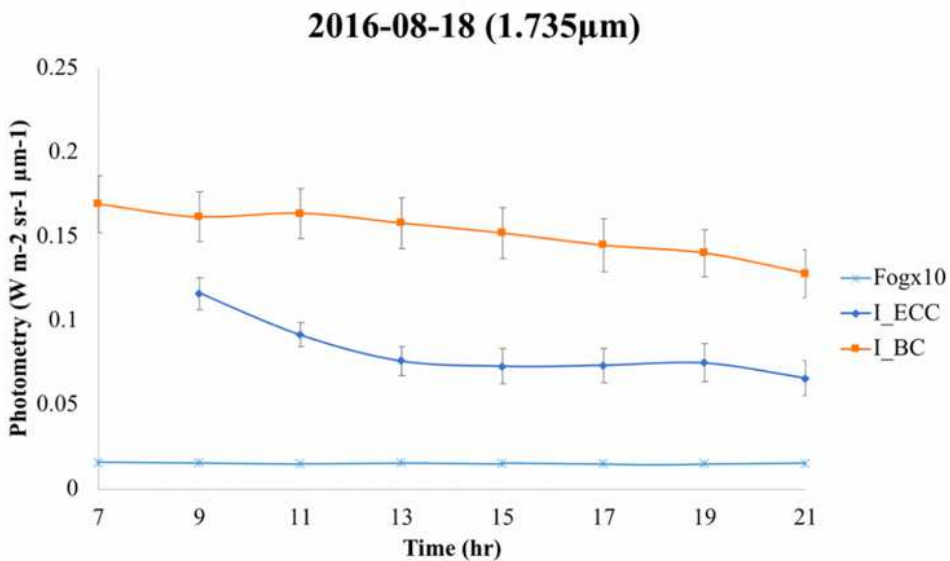
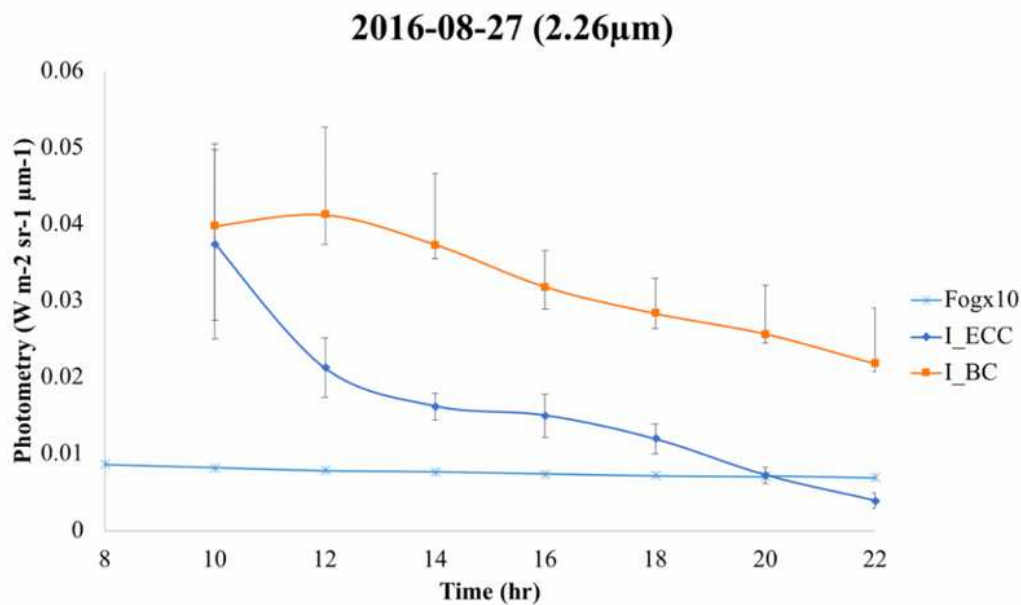


Figure 7

Average radiances of 'box region' in ECC and BC as selected in Figure 6a obtained for RDD images. Fogging factor x 10 range is included: (a) Aug-18 in $2.26\mu\text{m}$; (b) Aug-18 in $1.735\mu\text{m}$

(a) I_{ECC} and I_{BC} measurements from 10x10-region for 2016-08-27 RDD: 2.26 μm



(b) I_{ECC} and I_{BC} measurements from 10x10-region for 2016-08-27 RDD: 2.26 μm

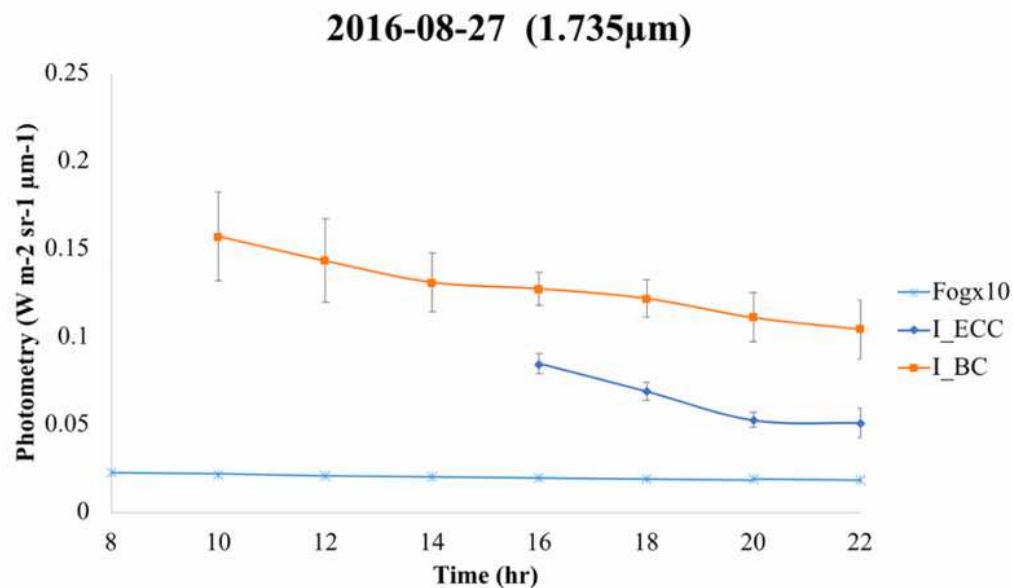


Figure 8

Average radiances of 'box region' in ECC and BC as selected in Figure 6b obtained for RDD images. Fogging factor x 10 range is included: (a) Aug-27 in 2.26 μm ; (b) Aug-27 in 1.735 μm

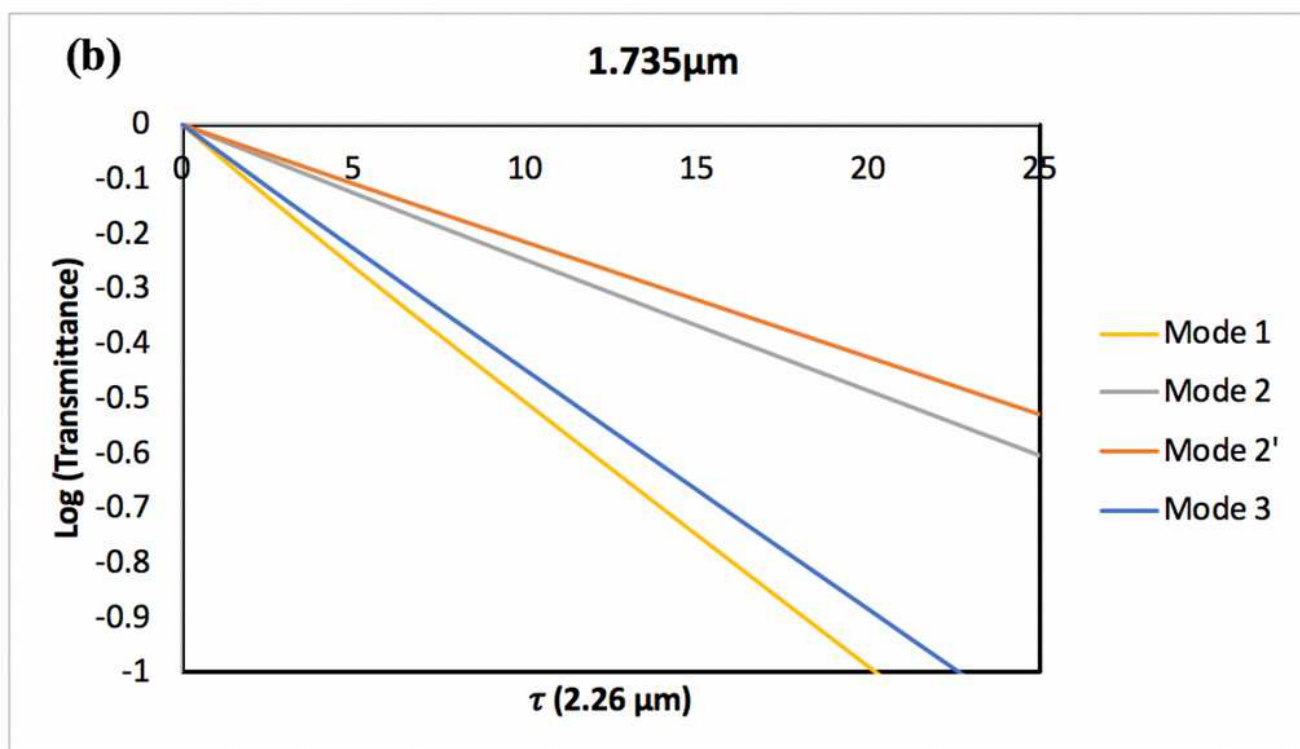
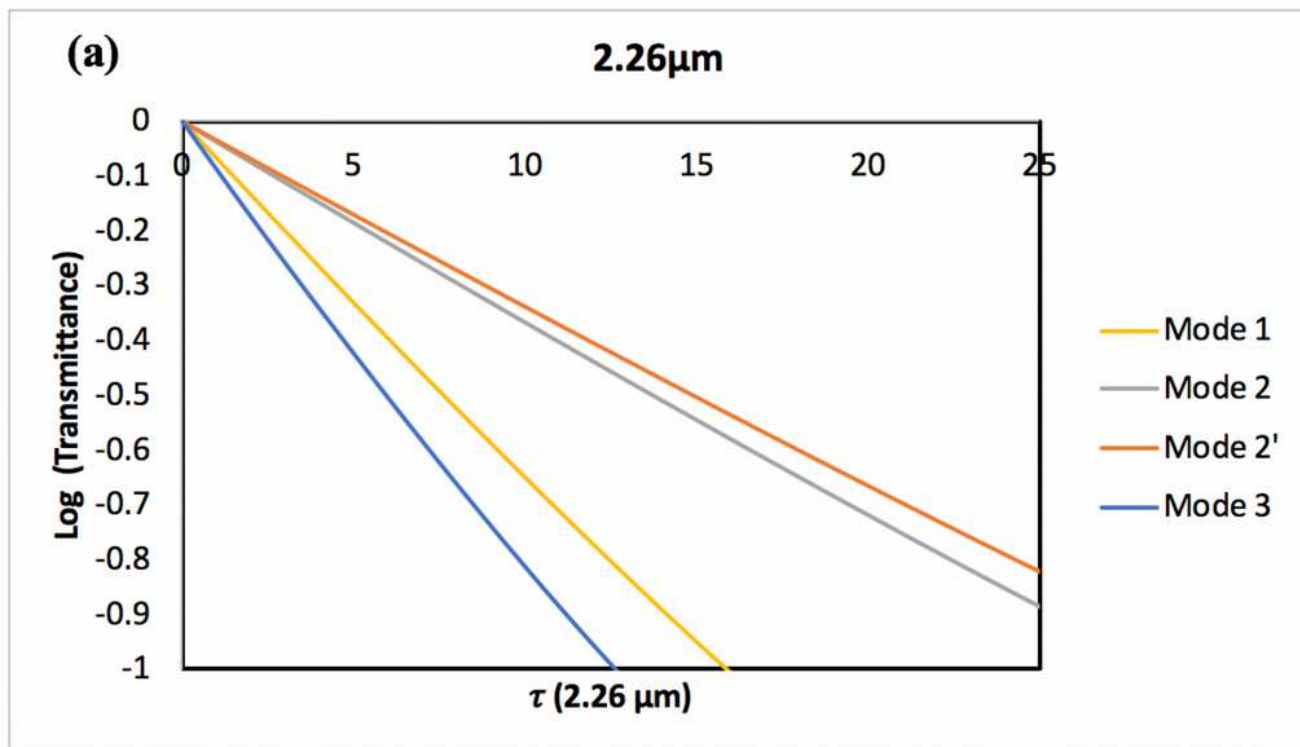


Figure 9

Radiative transfer calculation for transmittance by additional optical thickness of single-mode aerosols (mode 1, mode 2, mode 2', and mode 3) between 54 to 56 km altitude in: (a) 2.26 μm ; (b) 1.735 μm .

Observed TR over theoretical TR

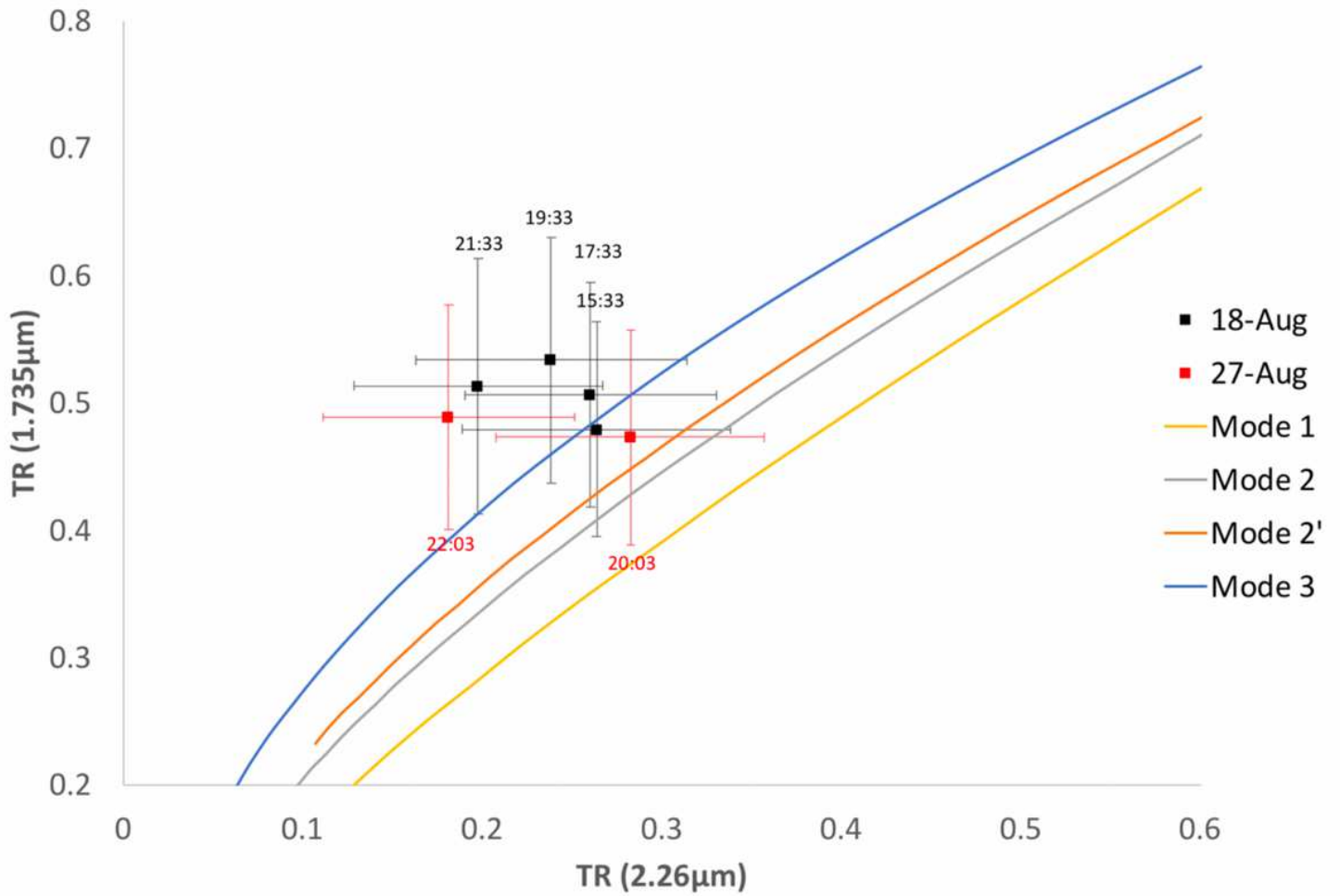


Figure 10

Observed Transmittance (TR) with associated uncertainty range plotting over theoretical Transmittance (TR) computed by radiative transfer for different particle size modes (mode 1, mode 2, mode 2', mode 3).

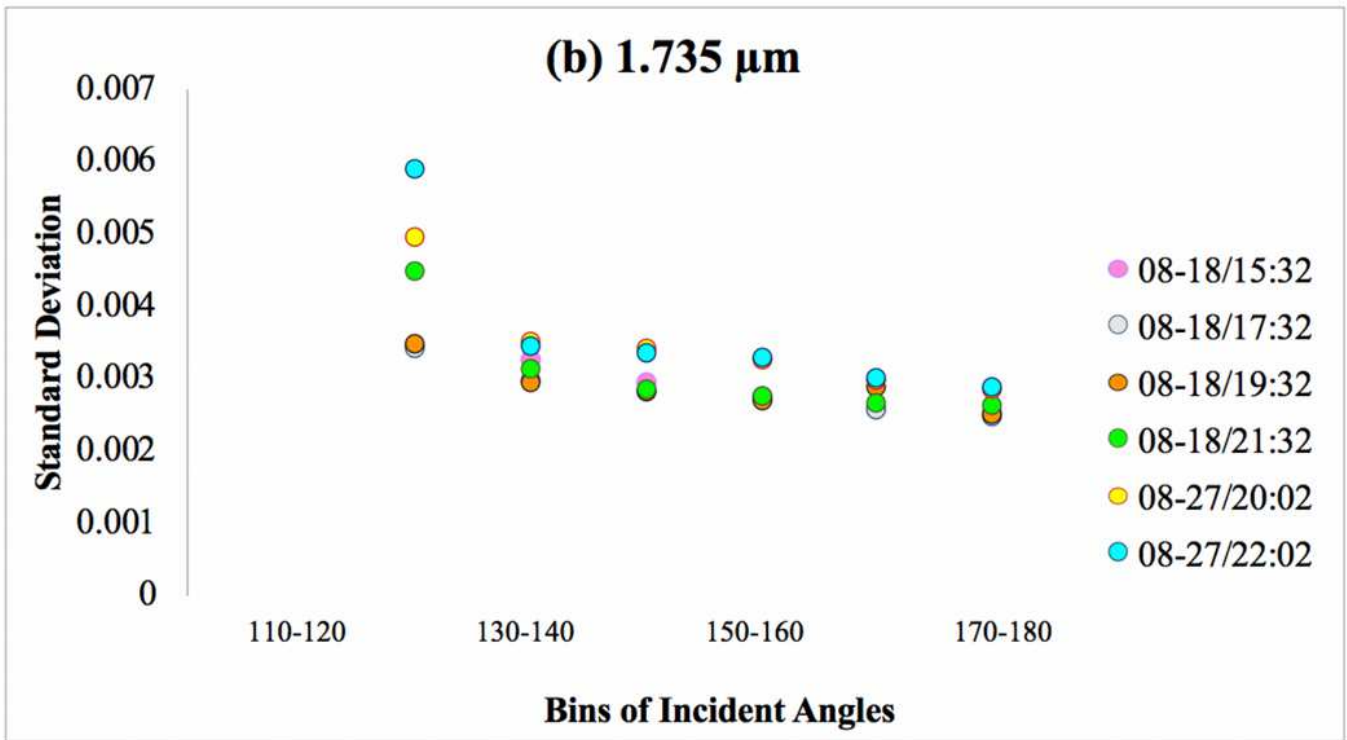
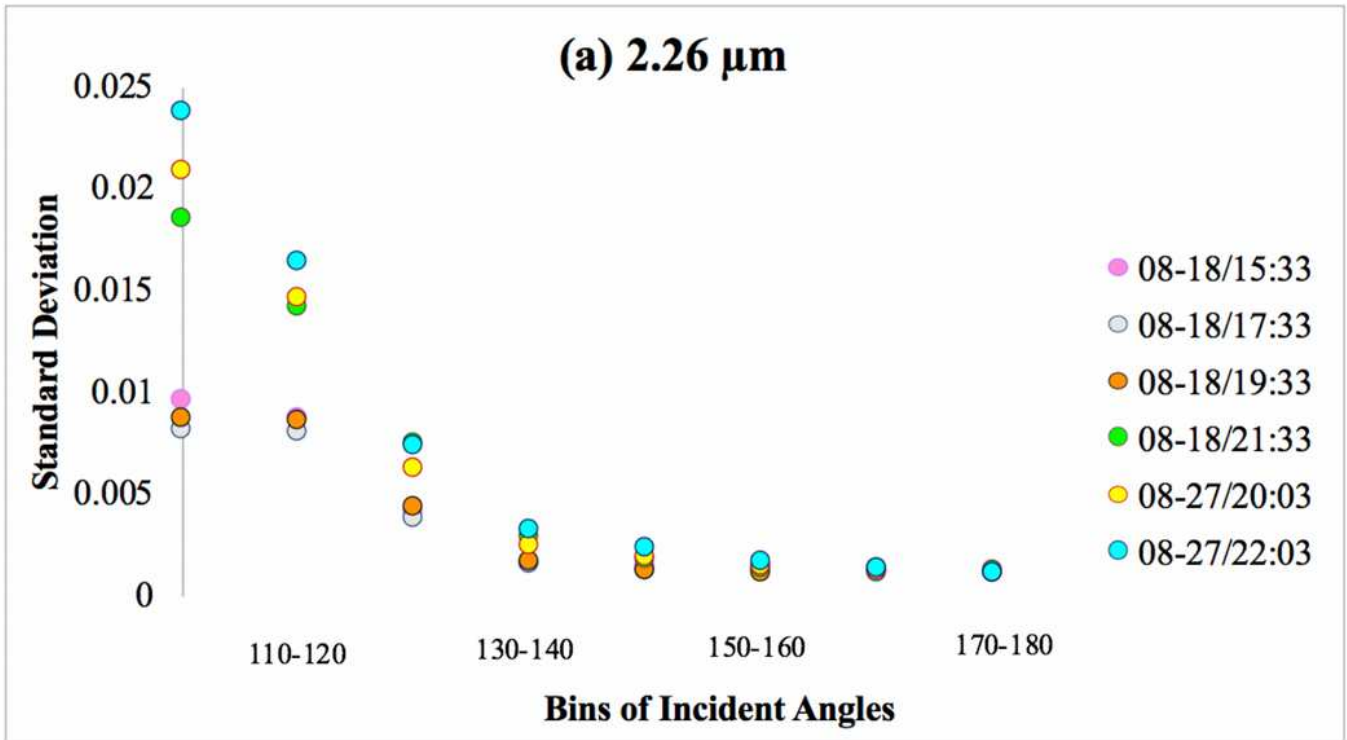


Figure 11

Standard deviation of CRD to L2B images in bins of 10° incident angles for: (a) $2.26\mu\text{m}$; (b) $1.735\mu\text{m}$. There are no data for incident angles before 120° due to saturation.

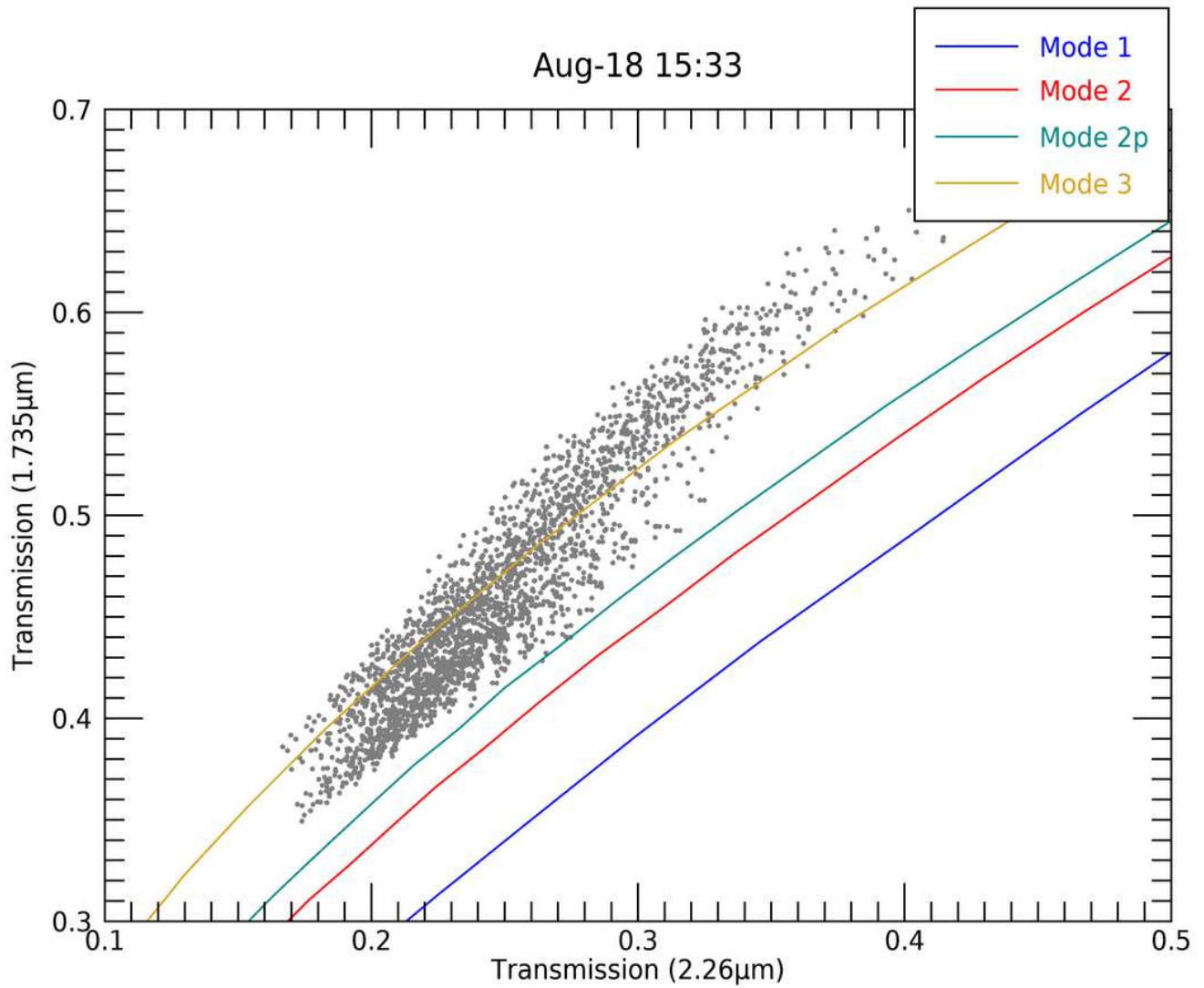


Figure 12

Total combinations of 4x4-regions' transmission ratios plotted over particle mode theoretical curves (mode 1, mode 2, mode 2' mode 3) showing alignment around mode 3 and slightly reaching mode 2' theoretical curves.

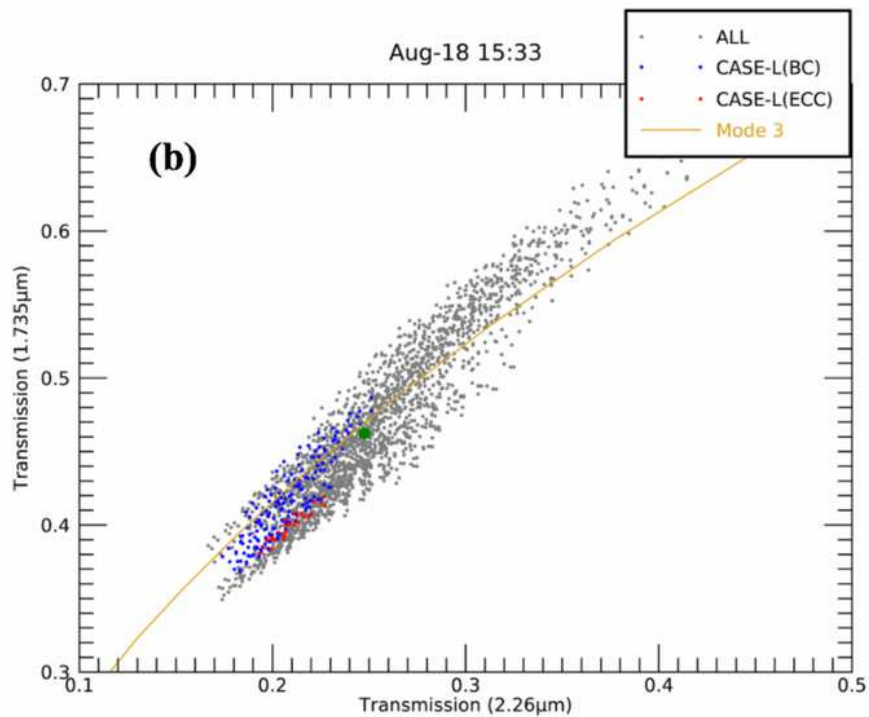
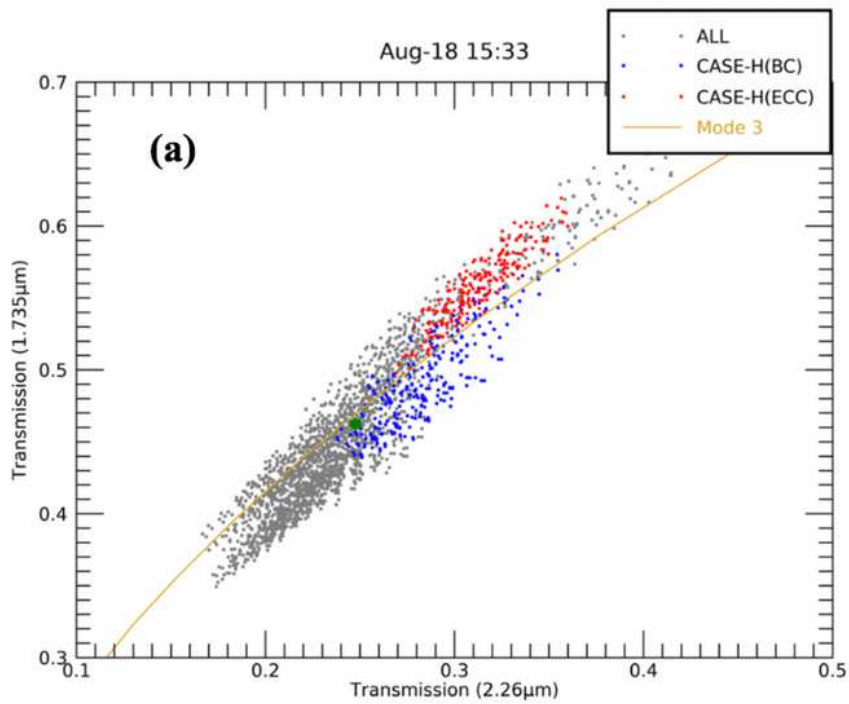


Figure 13

(a) Case-L in which to lower the transmissions. This is divided into two sub-groups. 'Case-L(BC)' where I_{BC} is brighter than 'normal' intensity and 'Case L(ECC)' where I_{ECC} is darker than normal intensity; (b) Case-H in which to increase to higher transmissions. This is divided into two sub-groups. 'Case-H(BC)' where I_{BC} is darker than 'normal' intensity and 'Case L(ECC)' where I_{ECC} is brighter than normal intensity

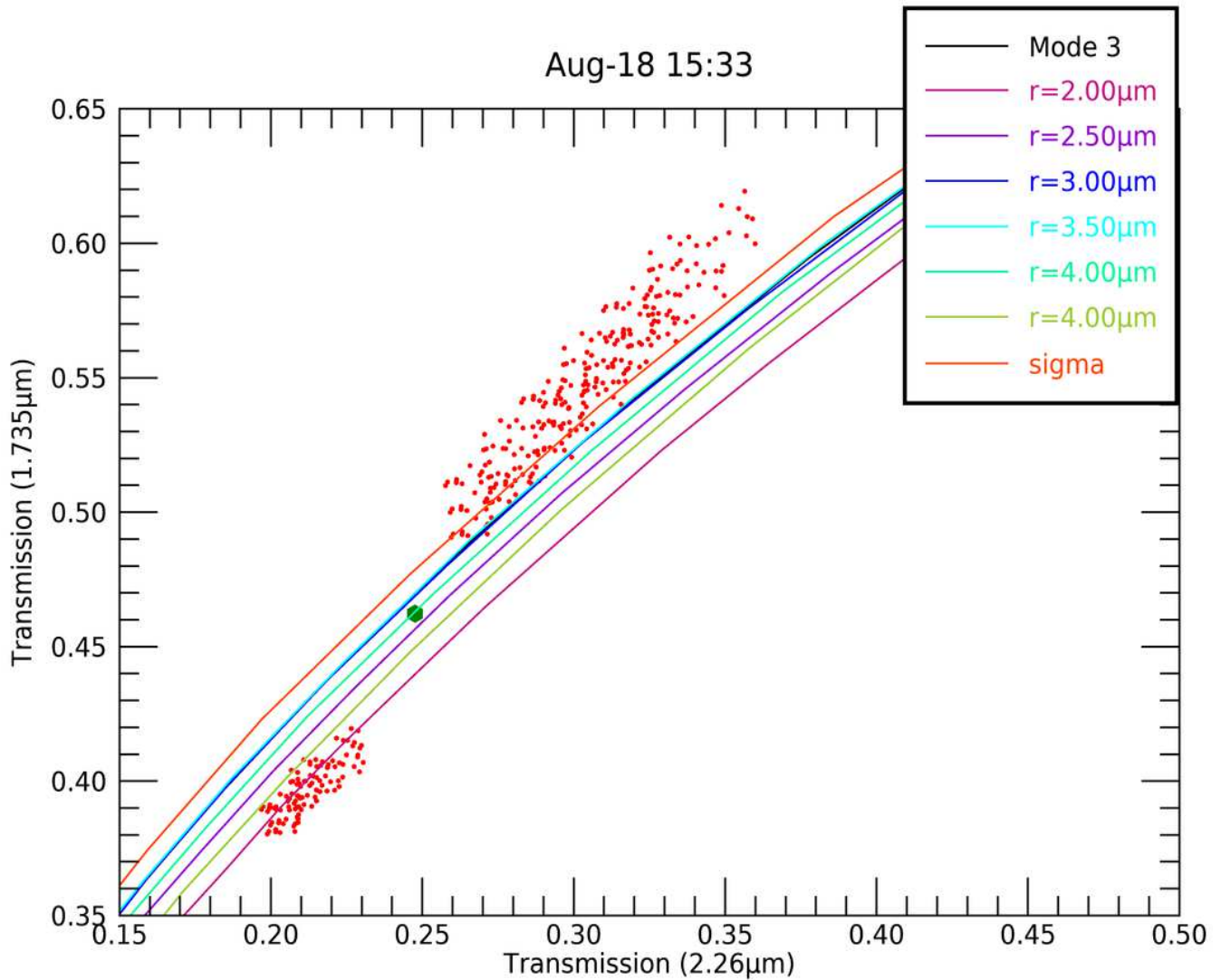


Figure 14

Theoretical transmittance calculated for mode 3' ranging from $r = 2.0\mu\text{m}$ to $4.5\mu\text{m}$ in $0.25\mu\text{m}$ intervals, and one fifth width of size distribution of mode 3 to the original denoted as '3.65 μm _sig', and mode 3 is 3.65 μm mean radius. (Red Dots) are from previous Figure 13a and 13b representing L_ECC points.

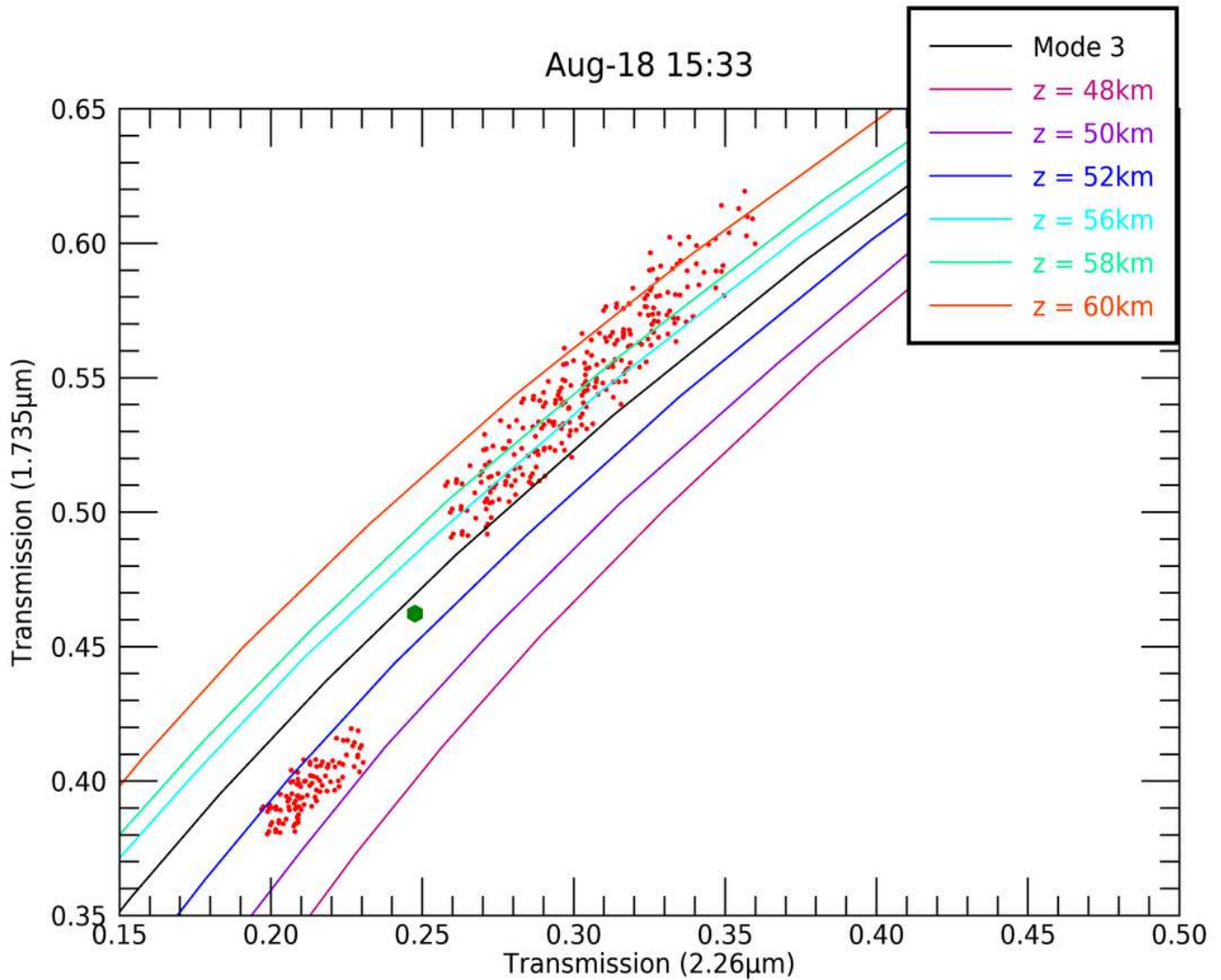


Figure 15

Radiative transfer calculations for emissions by single-mode aerosols (only mode 3 for this study) at different altitudes varying from 48-60km (at 2km intervals).

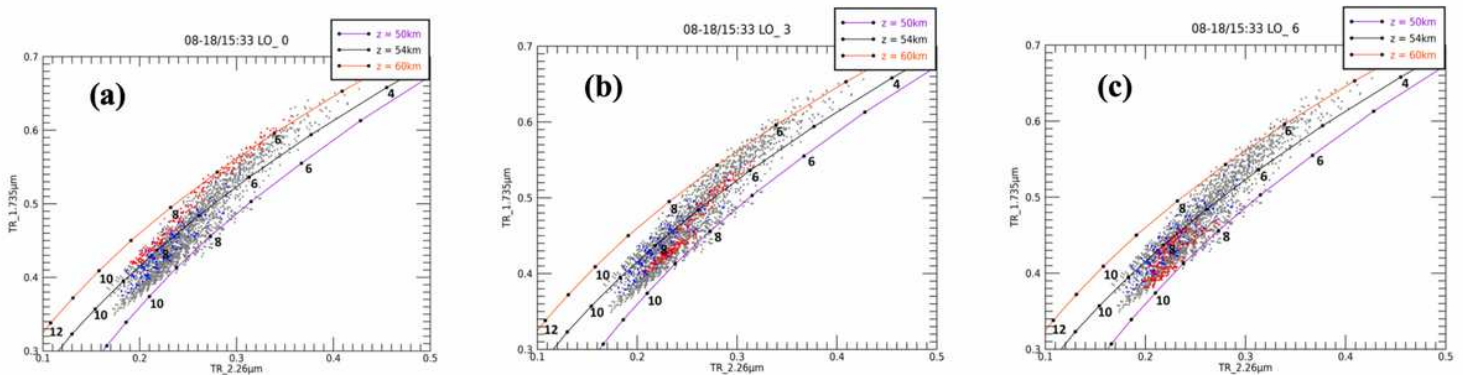


Figure 16

Combination scatter plots within 10x10region with resolution of 4x4-region statistical analysis. (Red) Transmission distribution of the Enormous Cloud Cover 'ECC'. (Blue) Transmission distribution of the Background Cloud 'BC' in 08-18/15:33: (a) LO_0, (b) LO_3, (c) LO_6

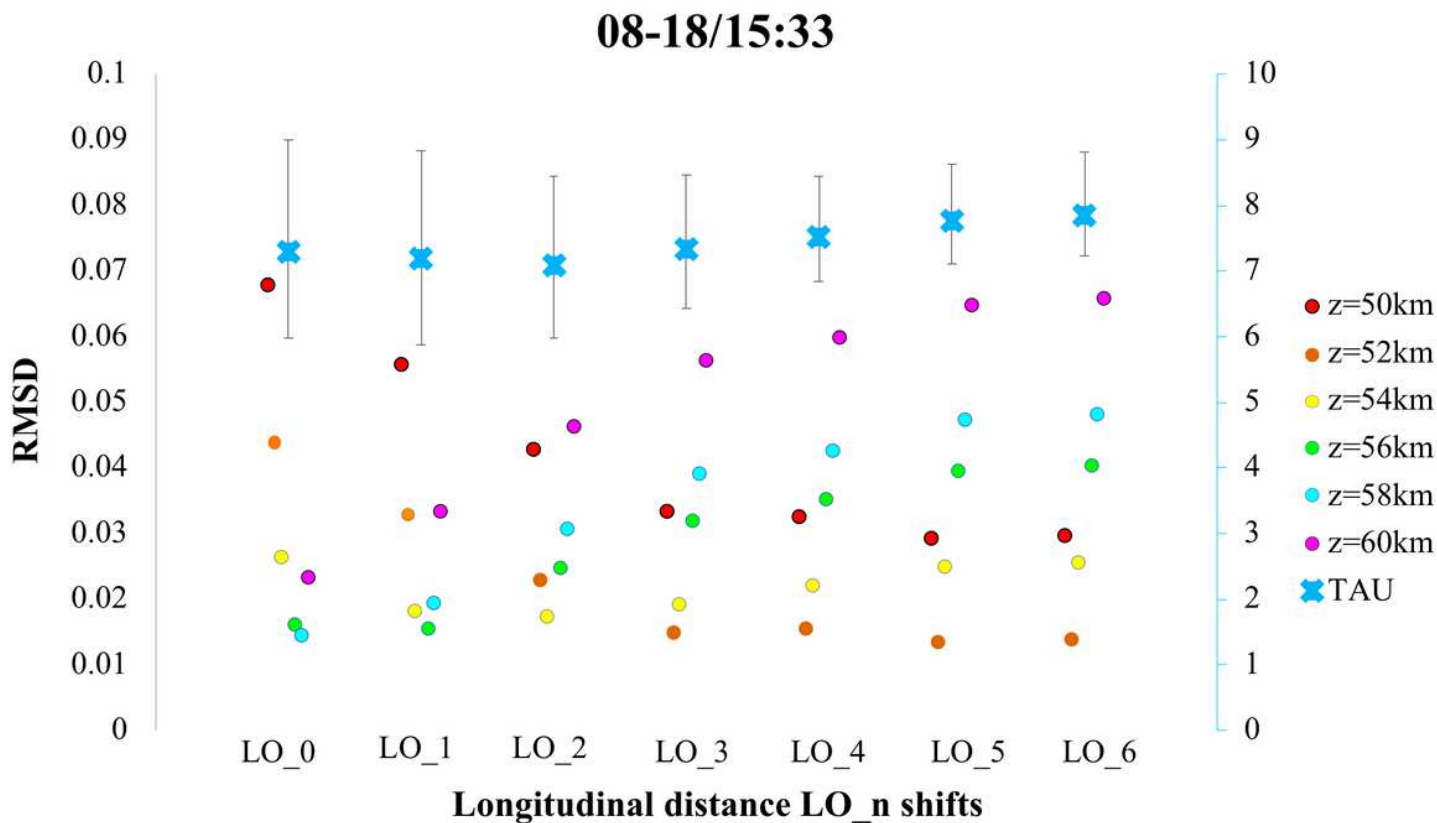


Figure 17

RMSD for longitudinal distance away from discontinuity front (spatial variation): 08-18/15:33. Left y-axis is RMSD and Right y-axis optical depths.

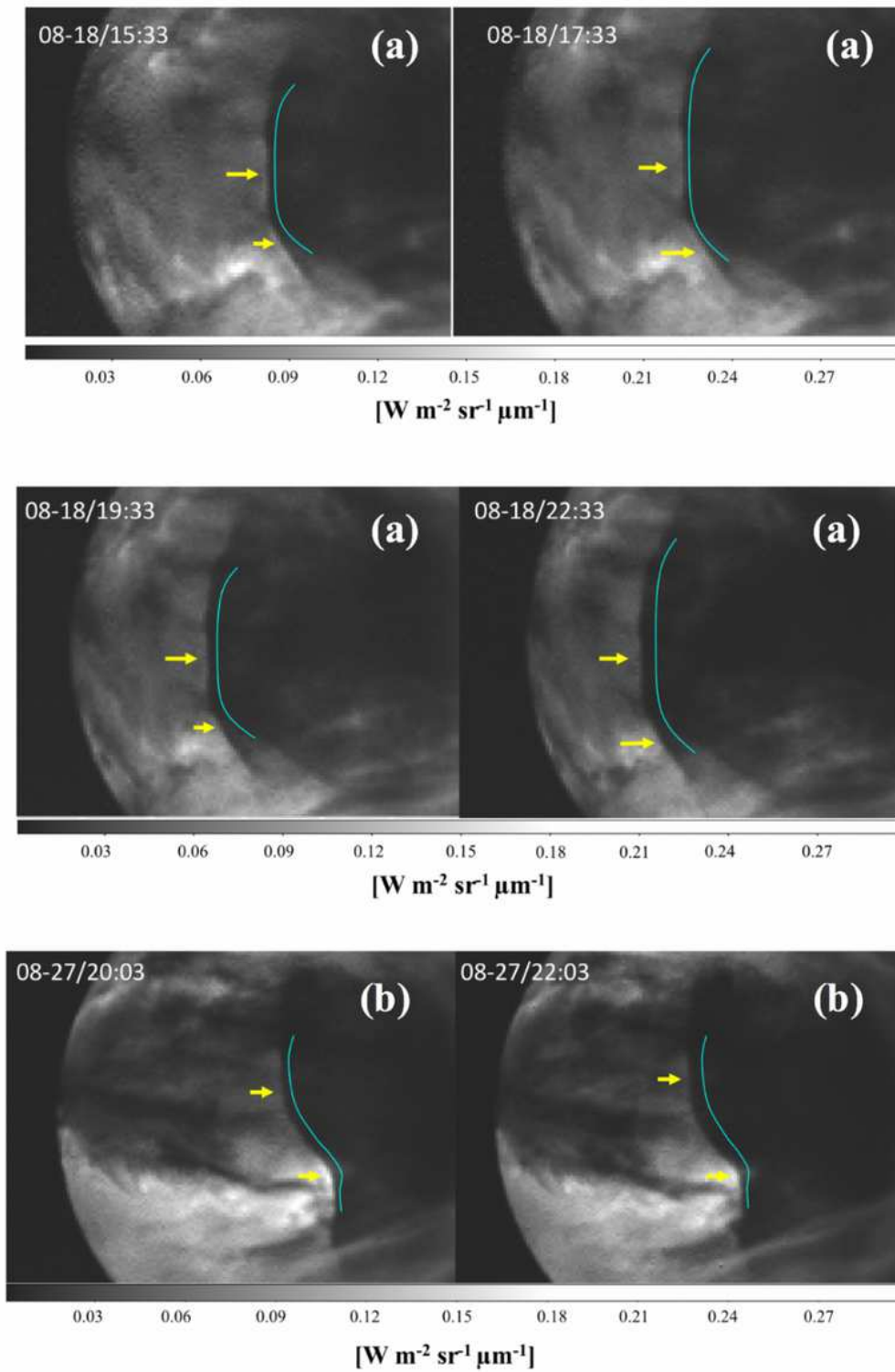


Figure 18

Close up image of RD-data (blue curve line) discontinuity front, (yellow arrow) bright downwelling features. (a) for 08-18/15:33, 17:33, 19:33, and 21:33. Note on the bright strip just after the front is most prominent at 15:33, then decreasing gradually in radiance to 21:33; (b) 08-27/20:03 and 22:03.

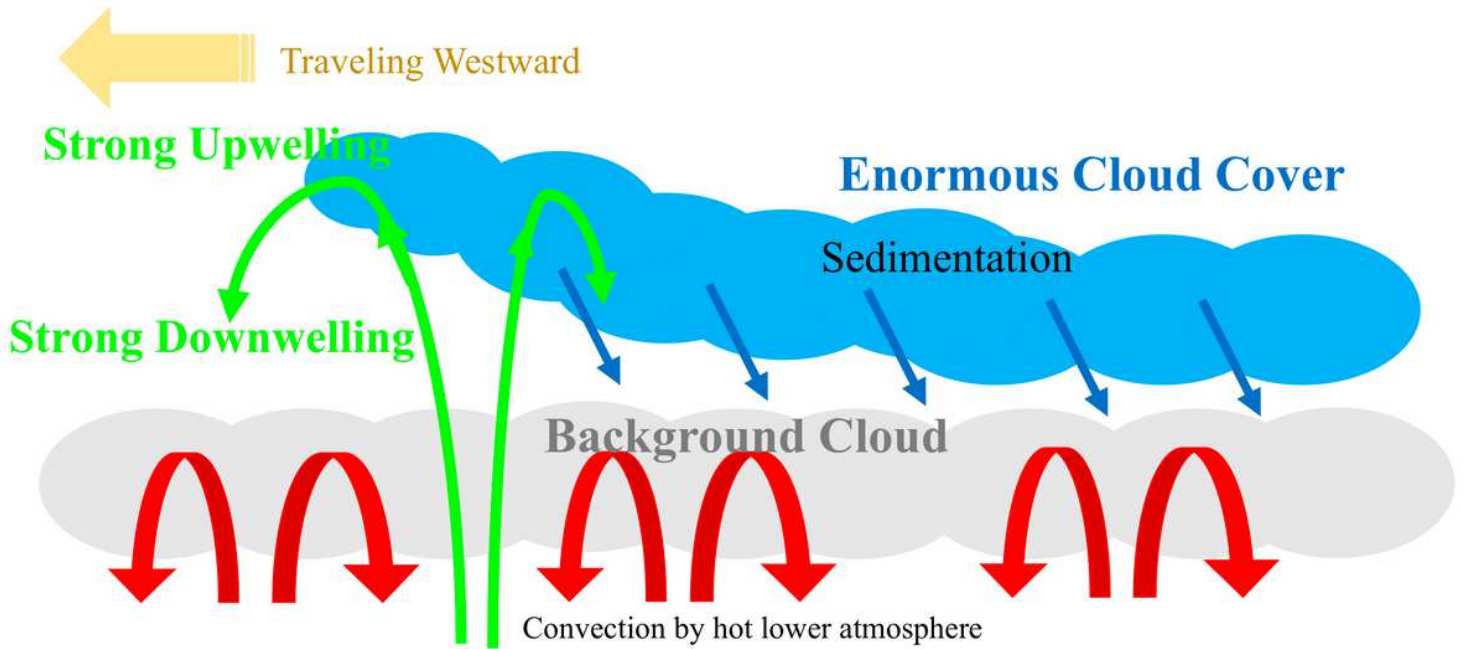


Figure 19

Schematics of ECC

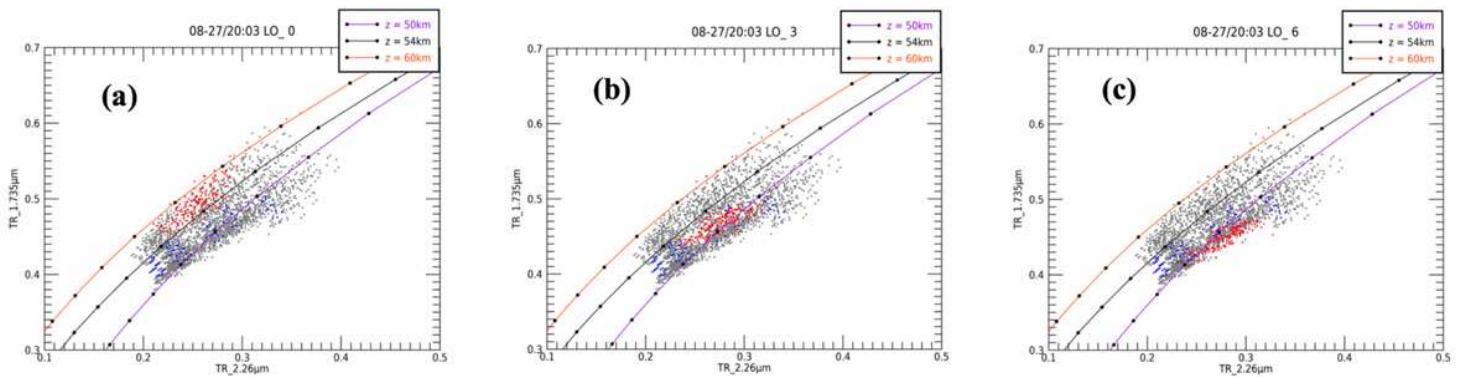


Figure 20

Combination scatter plots within 10x10region with resolution of 4x4-region statistical analysis. (Red) TR4 of the Enormous Cloud Cover 'ECC'. (Blue) Transmission distribution of the Background Cloud 'BC' in 08-27/20:03: (a) LO_0, (b) LO_3, (c) LO_6

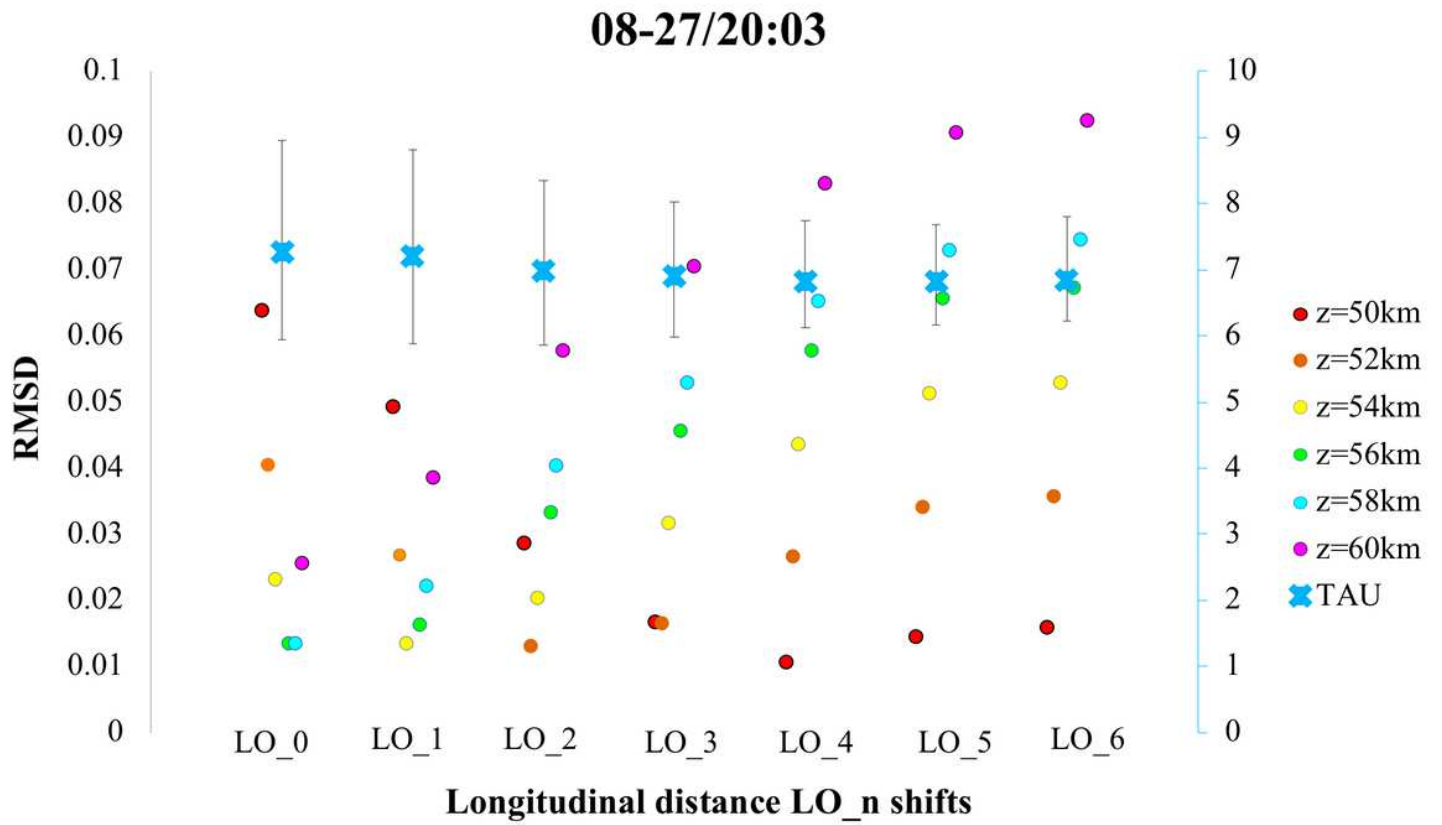


Figure 21

RMSD for longitudinal distance away from discontinuity front (spatial variation): 08-27/20:03. Left y-axis is RMSD and Right y-axis optical depths.

Supplementary Files

This is a list of supplementary files associated with this preprint. Click to download.

- [TablesVun.docx](#)